GLACE survey: OSIRIS/GTC tuneable filter Hα imaging of the rich galaxy cluster ZwCl 0024.0+1652 at z = 0.395

M. Sánchez-Portal, I. Pintos-Castro, R. Pérez-Martínez, J. Cepa,, A. M. Pérez García, H. Domínguez-Sánchez, A. Bongiovanni, A. L. Serra, E. Alfaro, B. Altieri, et al.

A&A 578, A30 (2015)
DOI: 10.1051/0004-6361/201525620

Astronomy & Astrophysics

GLACE survey: OSIRIS/GTC tuneable filter Hα imaging of the rich galaxy cluster ZwCl 0024.0+1652 at $z = 0.395$

I. Survey presentation, TF data reduction techniques, and catalogue*

M. Sánchez-Portal[1,2], I. Pintos-Castro[3,4,8,2], R. Pérez-Martínez[1,2], J. Cepa,[4,3], A. M. Pérez García[3,4], H. Domínguez-Sánchez[29], A. Bongiovanni[3,4], A. L. Serra[22,23], E. Alfaro[5], B. Altieri[1], A. Aragón-Salamanca[6], C. Balkowski[7], A. Biviano[9], M. Bremer[10], F. Castander[11], H. Castañeda[12], N. Castro-Rodríguez[3,4], A. L. Chies-Santos[25], D. Coia[1], A. Diaferio[23,24], P.A. Duc[13], A. Ederoclite[21], J. Geach[14], I. González-Serrano[15], C. P. Haines[16], B. McBreen[17], L. Metcalfe[1], I. Oteo[26,27], I. Pérez-Fournón[4,3], B. Poggianti[18], J. Polednikova[3,4], M. Ramón-Pérez[3,4], J. M. Rodríguez-Espinosa[4,3], J. S. Santos[28], I. Smail[19], G. P. Smith[17], S. Temporin[20], and I. Valtchanov[1]

(Affiliations can be found after the references)

Received 6 January 2015 / Accepted 10 February 2015

ABSTRACT

The cores of clusters at $0 \lesssim z \lesssim 1$ are dominated by quiescent early-type galaxies, whereas the field is dominated by star-forming late-type galaxies. Clusters grow through the accretion of galaxies and groups from the surrounding field, which implies that galaxy properties, notably the star formation ability, are altered as they fall into overdense regions. The critical issues for understanding this evolution are how the truncation of star formation is connected to the morphological transformation and what physical mechanism is responsible for these changes. The GaLAxy Cluster Evolution Survey (GLACE) is conducting a thorough study of the variations in galaxy properties (star formation, AGN activity, and morphology) as a function of environment in a representative and well-studied sample of clusters. To address these questions, the GLACE survey is making a deep panoramic survey of emission line galaxies (ELG), mapping a set of optical lines ([O II], [O III], Hβ and Hα/[N II] when possible) in several galaxy clusters at $z \sim 0.40$, 0.63, and 0.86. Using the tunable filters (TF) of the OSIRIS instrument at the 10.4 m GTC telescope, the GLACE survey applies the technique of TF tomography: for each line, a set of images are taken through the OSIRIS TF, each image tuned at a different wavelength (equally spaced), to cover a rest frame velocity range of several thousand km s^{-1} centred on the mean cluster redshift, and scanned for the full TF field of view of an 8 arcmin diameter. Here we present the first results of the GLACE project, targeting the Hα/[N II] lines in the intermediate-redshift cluster ZwCl 0024.0+1652 at $z = 0.395$. Two pointings have been performed that cover $\sim 2 \times r_{\rm vir}$. We discuss the specific techniques devised to process the TF tomography observations in order to generate the catalogue of cluster Hα emitters, which contains more than 200 sources down to a star formation rate (SFR) $\lesssim 1\ M_\odot$/yr. An ancillary broadband catalogue is constructed, allowing us to discriminate line interlopers by means of colour diagnostics. The final catalogue contains 174 unique cluster sources. The AGN population is distinguished using different diagnostics and found to be ~37% of the ELG population. The median SFR of the star-forming population is 1.4 $M_\odot$/yr. We studied the spatial distribution of ELG and confirm the existence of two components in the redshift space. Finally, we exploited the outstanding spectral resolution of the TF, attempting to estimate the cluster mass from ELG dynamics, finding $M_{200} = (4.1 \pm 0.2) \times 10^{14}\ M_\odot\,{\rm h}^{-1}$, in agreement with previous weak-lensing estimates.

Key words. galaxies: clusters: individual: ZwCl 0024.0+1652 – galaxies: photometry – galaxies: star formation – galaxies: active

1. Introduction

It is well known that, while the cores of nearby clusters are dominated by red early-type galaxies, a significant increase in the amount of blue cluster galaxies is observed at $z > 0.2$ (the so-called Butcher-Oemler (BO) effect; Butcher & Oemler 1984). An equivalent increase in obscured star formation (SF) activity has also been seen in the mid- and far-IR surveys of distant clusters (Coia et al. 2005; Geach et al. 2006; Haines et al. 2009; Altieri et al. 2010), as well as a growing population of active galactic nuclei (AGN; e.g. Martini et al. 2009, 2013). In general, a strong evolution (i.e. increase in the global cluster star formation rate, hereafter SFR) is observed (e.g. Webb et al. 2013; Koyama et al. 2011).

Even when focusing on a single epoch, aspects of this same evolutionary trend have been discovered in the outer parts of clusters where significant changes in galaxy properties can be clearly identified, such as gradients in typical colour or spectral properties with clustercentric distance (Balogh et al. 1999; Pimbblet et al. 2001) and in the morphology-density relation (Dressler 1980; Dressler et al. 1997). In a hierarchical model of structure formation, galaxies assemble into larger systems, namely galaxy clusters, as time progresses. It is quite likely that this accretion process is responsible for a transformation of the properties of cluster galaxies as a function of both redshift and environment (Balogh et al. 2000; Kodama & Bower 2001).

Haines et al. (2013) measured the mid-IR BO effect over the redshift range 0.0−0.4, finding a rapid evolution in the number of cluster massive ($M_K < -23.1$), luminous IR galaxies within r_{200} and $SFR > 3\ M_\odot$/yr that can be modelled as $f_{\rm SF} \propto (1+z)^n$,

* Table 5 is available in electronic form at http://www.aanda.org

with $n = 7.6 \pm 1.1$. The authors investigate the origin of the BO effect, finding that it can be explained as a combination of a ∼3× decline in the mean specific-SFR of star-forming cluster galaxies since $z \sim 0.3$ with a ∼1.5× decrease in number density. Two-thirds of this reduction in the specific-SFRs of star-forming cluster galaxies is due to the steady cosmic decline in the specific-SFRs amongst those field galaxies accreted into the clusters. The remaining one-third reflects an accelerated decline in the SF activity of galaxies within clusters. The slow quenching of SF in cluster galaxies is consistent with a gradual shut down of SF in infalling spiral galaxies as they interact with the cluster medium.

Possible physical processes that have been proposed to trigger or inhibit the SF include (e.g. Treu et al. 2003): (i) Galaxy-ICM interactions: ram-pressure stripping, thermal evaporation of the ISM, turbulent and viscous stripping, and pressure-triggered SF. When a slow decrease in the SF is produced, these mechanisms are collectively labelled as starvation. (ii) Galaxy-cluster gravitational potential interactions: tidal compression, tidal truncation. (iii) Galaxy-galaxy interactions: mergers (low-speed interactions), harassment (high-speed interactions). Nevertheless, it is still largely unknown whether the correlations of star-formation histories and large-scale structure are due to the advanced evolution in overdense regions or to a direct physical effect on the star formation capability of galaxies in dense environments (e.g. Popesso et al. 2007). This distinction can be made reliably if one has an accurate measurement of SFR (or history) for galaxies in different environments, spanning a range of stellar mass and redshift.

The physical processes proposed above act on the cluster population of emission line galaxies (ELG; comprising both SF and AGN population); narrow-band imaging surveys are very efficient at identifying *all* the ELGs in a cluster. For instance, Koyama et al. (2010) performed a MOIRCS narrow-band Hα and *Akari* mid-IR survey of the cluster RX J1716.4+6708 at $z = 0.81$, showing that both Hα and mid-IR emitters avoid the central cluster regions. A population of red SF galaxies (comprising both Hα and mid-IR emitters) is found in medium-density environments like outskirts, groups, and filaments, suggesting that dusty SF is triggered in the infall regions of clusters, implying a probable link between galaxy transition and dusty SF. The authors find that the mass-normalised cluster SFR declines rapidly since $z \sim 1$ as $\propto(1+z)^6$ (i.e. consistent with the results from Haines et al. 2013, outlined above).

"Classical" narrow-band imaging surveys have therefore demonstrated that they are a powerful tool, but they suffer from ambiguity about the true fluxes of detected sources and provide neither accurate membership nor dynamical information about the population. Attempting to overcome these limitations, but taking advantage of the power of narrow-band imaging, the GaLAxy Cluster Evolution Survey (GLACE) has been designed as an innovative survey of ELGs and AGNs in a well-studied and well-defined sample of clusters by exploiting the novel capabilities of the tunable filters (TF) of the OSIRIS instrument (Optical System for Imaging and low-Resolution Integrated Spectroscopy; Cepa et al. 2003, 2005) at the 10.4 m GTC telescope, to map a set of important optical emission lines by means of the technique of "TF tomography", which scans a range of the spectrum, i.e. a range of radial velocities around the cluster nominal redshift at a fixed wavelength step.

The main purpose of this paper is to present the GLACE project, along with some specific techniques devised to process TF data and the results of several simulations performed to assess the quality and performance of the observations and procedures developed. In addition, results from the Hα/[N II] survey performed in the galaxy cluster ZwCl 0024+1652 (hereafter referred to as Cl0024) at $z = 0.395$ are presented. In Sect. 2, the GLACE survey is outlined, including its main objectives, technical implementation, and intended targets. Then, Sect. 3 reports on the observations towards Cl0024, along with the procedures developed to reduce TF data within the GLACE survey. The method for flux calibration is also addressed, as is Cl0024 ancillary broadband data and spectroscopic redshifts. In Sect. 4 the methods for deriving the catalogue of ELG, including line wavelength estimation and rejection of contaminants (line emitters at different redshifts) are described. Section 5 addresses the derivation of the Hα and [N II] fluxes and possible explanations to the absorption-like features observed in some cases in the spectral data. In Sect. 6 we discuss the spatial and redshift distribution of the cluster galaxies. Section 7 is dedicated to the Hα luminosity function of Cl0024 and to its comparison with previous work (Kodama et al. 2004). In Sect. 8, the distinction between star-forming galaxies and AGNs is discussed. Finally, Sect. 9 investigates the possibility of studying the dynamical properties of clusters of galaxies by means of emission (rather than absorption) lines.

This is first in a series of papers on the GLACE targets. A thorough discussion of the SF properties of Cl0024 derived from the Hα line and their comparison with mid- and far-IR results, as well as discussion of the results derived from the rest of the targeted lines will be addressed in forthcoming papers (Pérez-Martínez et al., in prep.). The IR-derived SF properties of the young galaxy cluster RX J1257.2+4738 at $z = 0.866$ (see GLACE target list below) have been discussed in Pintos-Castro et al. (2013). The GLACE [O II] OSIRIS TF survey of this cluster and the morphological properties of the star-forming and AGN population are being addressed in Pintos-Castro et al. (in prep.).

Unless otherwise specified, throughout this paper we assume a Universe with $H_0 = 70\,\mathrm{km\,s^{-1}\,Mpc^{-1}}$, $\Omega_\Lambda = 0.7$, and $\Omega_\mathrm{m} = 0.3$.

2. The GLACE project

The GLACE programme (PIs. Miguel Sánchez-Portal & Jordi Cepa) is undertaking a panoramic census of the SF and AGN activity within a sample of clusters at three redshift bins defined by windows relatively free of strong atmospheric OH emission lines (Fig. 1): $z \sim 0.40$, 0.63, and 0.86, mapping the strongest rest-frame optical emission lines: Hα (only at $z \sim 0.4$), Hβ, [OII]3727, and [OIII]5007. The sections below describe the main goals of the GLACE project and the technical implementation of the project.

2.1. GLACE goals

The GLACE project is aimed at comparing the maps of ELGs with the structures of the targeted clusters (as traced by galaxies, gas, and dark matter) to address several crucial issues.

(1) Star formation in clusters: We determine how the SF properties of galaxies relate to their position in the large scale structure. This will provide a key diagnostic for testing between different models for the environmental influence on galaxy evolution. Each mechanism is most effective in a different environment (generally depending on the cluster-centric distance, e.g. Treu et al. 2003), and it leaves a footprint in the data. We are mapping the extinction-corrected SF through Hα and [OII], over a large and representative region in a

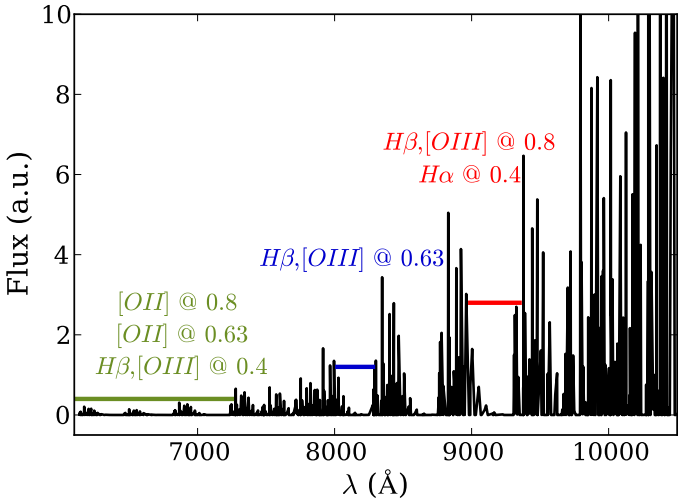

Fig. 1. Night sky spectrum from Rousselot et al. (2000) and GLACE windows within the OH bands. The locii of the strongest rest-frame emission lines at different redshifts are shown next to the corresponding spectral windows. The observations within this paper have been performed within the Hα window at $z = 0.4$.

statistically useful sample of clusters. The survey has been designed to reach $SFR \sim 2\ M_{\odot}$/yr (i.e. below that of the Milky Way) with one magnitude of extinction at Hα[1]. Our first results (see Sect. 4) show that we are achieving this goal. Another important question that can be addressed is related with the kind of galaxies (type/mass) forming stars within clusters. The study of the morphology of confirmed ELGs allows investigating the connection between the truncation of SF and the morphological transformation of infalling galaxies (e.g. Poggianti et al. 1999). In addition, by determining the total integrated SFRs, we can construct a SF history for galaxies in clusters, as has been done in the field (e.g. Madau et al. 1998).

(2) The role of AGNs: Whether the fraction of AGNs depends on environment is a matter of debate: while some results (e.g. Miller et al. 2003) point towards a lack of dependency of the AGN fraction on the local galaxy density, other authors (e.g. Kauffmann et al. 2004) conclude that high-luminosity AGNs do avoid high-density regions. Such a lack of AGNs in clusters, as compared to the field, may be related to the evolution of galaxies as they enter the cluster environment. On the other hand, claims for a larger percentage of AGNs in groups (e.g. Popesso & Biviano 2006) point to AGN-stimulating processes, such as galaxy–galaxy interactions or mergers, that are particularly effective in the low-velocity dispersion and (relatively) high-density environments typical of groups (and filaments).
Regarding redshift evolution, Martini et al. (2009, 2013) have studied the number of luminous AGNs in clusters up to $z \simeq 1.5$, finding 30 times more at $1 < z < 1.5$ than found in clusters at $z \sim 0.25$ and more than one order of magnitude more than found at $z \sim 0.75$, indicating that the AGN population in clusters has evolved more rapidly than the field one, analogous to the faster evolution of cluster SF galaxies with respect to field.
A complete census of the AGN population in clusters at different redshifts and in cluster regions characterised by different mean densities and velocity dispersions can help us to constrain the physics behind the onset of the AGN activity in galaxies. Our survey is sensitive to the AGN population within clusters, differentiated from pure SF by means of standard diagnostics, e.g. BPT (Baldwin et al. 1981) and EWαn2 (Cid Fernandes et al. 2010) diagrams.

(3) The study of the distribution of galaxy metallicities with cluster radii is another powerful way to investigate evolution within clusters. As galaxies fall into clusters and travel towards the cluster centre along their radial orbits, they interact with the intra-cluster medium (ICM) and other cluster galaxies, thus getting progressively stripped of their gas reservoir. This process is expected to influence their metal abundances and possibly generate a metallicity gradient across a cluster. Not much is known yet about the metallicity of emission line galaxies in clusters and how it varies with cluster-centric distances. GLACE will allow extinction-corrected metallicities to be derived using N2 (Denicoló et al. 2002), R23 (Pagel et al. 1979) and O3N2 (Alloin et al. 1979), where N2 and O3N2 will be used to break the R23 degeneracy and to assess possible differences between N and O abundances vs. metallicity.

The survey addresses many other interesting topics: for instance, the cluster accretion history can be traced by studying the census of ELGs at different cluster-centric distances. In addition, the survey will provide an accurate assessment of cluster membership, without the need of a spectroscopic follow-up.

2.2. GLACE implementation and TF principles

Regarding the technical implementation, the GLACE survey exploits the outstanding characteristics of the tunable filters (TF; González et al. 2014; Cepa et al. 2005, 2003); these are special Fabry-Perot interferometers in which the two plane parallel transparent plates (covered with high-reflectivity, low-absorption coatings) are operated at much smaller spacing than the traditional ones (typically a few microns). As a result, a broadened central interference region is produced (known as the Jacquinot spot, defined as the region over which the change in wavelength does not exceed $\sqrt{2} \times FWHM$). Moreover, controlled by means of a stack of piezo-electric transducers, the plate spacing can be varied with high accuracy over a wide range. Therefore, a broad spectral region is accessible with a moderate spectral resolution (about 10–20 Å FWHM). In the case of the OSIRIS red TF, the spectral range is 6510–9345 Å.

The TF transmission profile (Airy function) is periodic with the incident light wavelength. For a beam entering the TF at incidence angle θ, the condition for a maximum transmission (constructive interference) is

$$m\lambda = 2\mu d \cos\theta \quad (1)$$

where m is the integer order of interference, μ the refractive index of the medium in the cavity between the plates (usually air, $\mu = 1$), and d the plate separation (gap). To select just one wavelength and order, additional intermediate-band filters, known as order sorters, are required. Since light coming from targets at increasing distance from the OSIRIS optical centre reaches the TF at increasing incidence angle, there is a progressive shift towards the blue as the distance r of the source to the optical centre increases. For the OSIRIS red TF, the dependency of the transmitted wavelength on the radial distance is given by González et al. (2014):

$$\lambda = \lambda_0 - 5.04r^2 + a_3(\lambda)r^3 \quad (2)$$

[1] $f_{\mathrm{H}\alpha} = 1.89 \times 10^{-16}$ erg s^{-1} at $z = 0.4$ using standard SFR-luminosity conversion factors (Kennicutt 1998).

Table 1. GLACE sample and status of the observations.

Name	RA(J2000)	Dec(J2000)	z	Status
ZwCl 0024.0+1652	00 26 35.7	+17 09 45	0.395	Completed; programmes GTC63-09B, GTC8-10AGOS, GTC47-10B & GTC75-13B
Abell 851	09 42 56.6	+46 59 22	0.407	Planned
RX J1416.4+4446	14 16 28.7	+44 46 41	0.40	Planned
XMMLSS-XLSSC 001	02 24 57.1	−03 48 58	0.613	Planned
MACS J0744.8+3927	07 44 51.8	+39 27 33	0.68	Planned
Cl J1227.9-1138	12 27 58.9	−11 35 13	0.636	Planned
XLSSC03	02 27 38.2	−03 17 57.0	0.839	Planned
RX J1257.2+4738	12 57 12.2	+47 38 07	0.866	Completed; ESO/GTC programme 186.A-2012
Cl 1604+4304	16 04 23.7	+43 04 51.9	0.89	Planned; Cl 1604 supercluster

where λ_0 is the central wavelength tune in Å, r the distance to the optical centre in arcmin, and $a_3(\lambda)$ is an additional term expressing the wavelength dependency of the coatings, given by

$$a_3(\lambda) = 6.0396 - 1.5698 \times 10^{-3}\lambda + 1.0024 \times 10^{-7}\lambda^2. \quad (3)$$

Within a wavelength period, the TF transmission profile $T(\lambda)$ can be approximated by the expression:

$$T(\lambda) \simeq \left(1 + \left(\frac{2(\lambda - \lambda_0)}{\Delta_{\rm FWHM}}\right)^2\right)^{-1} \quad (4)$$

where λ_0 is the wavelength at which the TF is tuned, and $\Delta_{\rm FWHM}$ is the TF FWHM bandwidth.

Within the GLACE survey, we applied the technique of TF tomography (Jones & Bland-Hawthorn 2001; Cepa et al. 2013): for each line, a set of images are taken through the OSIRIS TF, each image tuned at a different wavelength (equally spaced), so that a rest frame velocity range of several thousand km s^{-1} (6500 km s^{-1} for our first target) centred on the mean cluster redshift is scanned for the full TF field of view of 8 arcmin in diameter. Additional images are taken to compensate for the blueshift of the wavelength from the centre to the edge of the field of view (as given in Eq. (2)). Finally, for each pointing and wavelength tuned, three dithered exposures allow correcting for etalon diametric ghosts, using combining sigma clipping algorithms.

The TF FWHM and sampling (i.e. the wavelength interval between consecutive exposures) at Hα are of 12 and 6 Å, respectively, to allow deblending Hα from [N II]λ6584. with an accuracy better than 20% (Lara-López et al. 2010). For the rest of the lines, the largest available TF FWHM, 20 Å is applied, with sampling intervals of 10 Å. These parameters also allow a photometric accuracy better than 20% according to simulations performed within the OSIRIS team. The same pointing positions are observed at every emission line. To trace the relation between SF and environment in a wide range of local densities, we required ≃2 Virial radii (some 4 Mpc) to be covered within the targeted clusters. This determines the number of OSIRIS pointings (two pointings at 0.40 and 0.63 and just one at 0.86).

The intended GLACE sample includes nine clusters, three in each redshift bin. Currently we have been awarded with observing time and completed the observations of clusters: ZwCl 0024.0+1652 and RX J1257.2+4738. Table 1 outlines the sample and the current status of the observations.

3. Observations and data reduction

Two OSIRIS/GTC pointings using the red TF were planned and executed towards Cl0024. The first one (carried out in GTC semesters 09B, 10A, and 13B; hereafter referred to as "centre position") targeted the Hα/[N II], Hβ and [O III] lines. The observations were planned to keep the cluster core well centred within CCD1[2]. The second pointing (hereafter referred to as "offset position") was carried out in semesters 10B and 13B, and it targeted the same emission lines. This second pointing was offset by $\Delta\alpha = -2.3$ arcmin, $\Delta\delta = +2.5$ arcmin (i.e. some 3.4 arcmin in the NW direction). A summary of the observations is presented in Table 2. Within the scope of this paper, we present the results from the Hα/[N II] observations. The total on-source exposure time is 5.1 and 2.9 h at the central and offset pointings, respectively.

The Hα/[N II] spectral range 9047–9341 Å was covered by 50 evenly spaced scan steps[3] ($\Delta\lambda = 6$ Å). Taking the radial wavelength shift described by Eq. (2) into account, the spectral range sampled over the entire field of view (of 8 arcmin diameter) is somewhat smaller, 9047−9267 Å. (The ranges 9267−9341 Å and 8968−9047 Å are partially covered in the central and external regions of the field of view, respectively.) At each TF tune, three individual exposures with an "L-shaped" dithering pattern of 10 arcsec amplitude were taken (to allow the removal of fringes and to ease the identification of diametric ghosts; the amplitude was chosen similar to the gap between the detectors). While this observing strategy has revealed itself to be useful for removing the fringing patterns that are especially evident beyond $\lambda \simeq 9300$ Å, it introduces an additional complexity since the position of a source within the CCD varies in each dither position and as a consequence also the wavelength at which it is observed owing to the radial wavelength shift experienced in TFs.

3.1. TF data reduction procedures

The data was reduced using a version of the TFRED package Jones et al. (2002) modified for OSIRIS by A. Bongiovanni (Ramón-Pérez et al., in prep.) and private IRAF[4] and IDL scripts written by our team. The basic reduction steps were carried out using standard IRAF procedures and included bias subtraction and flat-field normalisation. The next reduction step was a

[2] The OSIRIS detector mosaic is composed of two 2048 × 4096 pixel CCDs abutted, with a plate scale of 0.125 arcsec/pixel. See Cepa et al. (2005) and the OSIRIS Users' manual at http://www.gtc.iac.es/instruments/osiris/media

[3] Three scan steps, at 9317.4 and 9323.4 and 9341.4 Å were accidentally omitted in the observations of the offset positions, so only 47 slices are available for that pointing.

[4] IRAF is distributed by the National Optical Astronomy Observatory, which is operated by the Association of Universities for Research in Astronomy (AURA) under cooperative agreement with the National Science Foundation.

Table 2. Log of the OSIRIS/TF observations of the region centred around the Hα emission line in the Cl0024 cluster.

Centre position						
$\lambda_{0,i}$ (nm)	OS filter	Date	Seeing ($''$)	N steps	N exp.	Exp. time (s)
904.74	f893/50	2009 Dec. 05	0.7–0.9	6	3	53
		2010 Aug. 17	0.8	6	3	85
908.34	f902/40	2010 Aug. 21	0.8	11	3	60
908.74	f902/40	2009 Dec. 05	0.7–0.9	2	3	53
909.54	f902/40	2009 Nov. 25	0.9–1.1	9	3	53
914.94	f910/40	2009 Nov. 25	0.9–1.1	9	3	53
		2010 Aug. 01	0.8	14	3	60
920.34	f910/40	2009 Dec. 05	0.6–0.8	5	3	53
923.34	f919/41	2009 Dec. 05	0.6–0.8	4	3	53
		2010 Aug 18	0.8	3	3	60
925.14	f919/41	2010 Aug. 18	0.8	5	3	100
928.14	f919/41	2010 Aug. 18	0.8	3	3	120
929.94	f919/41	2010 Aug. 19	0.9	3	3	190
931.74	f923/34	2010 Aug. 19	0.9	2	3	170
932.94	f923/34	2010 Aug. 21	0.8	3	3	120
Offset position						
$\lambda_{0,i}$ (nm)	OS filter	Date	Seeing ($''$)	N steps	N exp.	Exp. time (s)
904.74	f893/50	2010 Oct 01	<1.0	6	3	60
908.34	f902/40	2010 Nov. 08	1.0–1.2	11	3	60
914.94	f910/40	2010 Sep. 20	<0.8	14	3	60
923.34	f919/41	2010 Nov. 08	0.9–1.2	3	3	60
925.14	f919/41	2010 Nov. 08	0.9–1.2	5	3	100
928.14	f919/41	2010 Nov. 08	0.9–1.2	3	3	120
929.94	f919/41	2010 Nov. 08	1.0–1.2	3	3	120
932.94	f923/34	2010 Oct. 01	<1.0	2	3	120

TF-specific one, namely the removal of the diffuse, optical-axis centred sky rings produced by atmospheric OH emission lines as a consequence of the radial-dependent wavelength shift described by Eqs. (2) and (3).

The TFRED task `tringSub2` was used to this end. It corrects each individual exposure by means of a background map created by computing the median of several dithered copies of the object-masked image. Fringing was also removed when required using the dithered images taken with the same TF tune. Then, the frames were aligned and a deep image obtained by combining all individual exposures of each scan step. This combination was achieved by applying a median filter. While this could potentially lead to the loss of line emitters with a very low continuum level, it is the best method of removing spurious features as ghosts.

When we compared the deep image resulting from the procedure described above with that obtained by adding up all the individual scans and applying a simple minimum-maximum rejection filter, we observed that one line emitter per CCD at most gets lost, but more than one hundred spurious features are removed effectively. The astrometry was performed in the resulting deep image, using IRAF standard tasks (`ccxymatch` and `ccmap`). The sky position of reference objects were gathered from the USNO B1.0 catalogue (Monet et al. 2003) in the centre position, while for the offset one we obtained better results using the 2MASS catalogue (Skrutskie et al. 2006); the achieved precision was in both cases equal to or better than 0.3 arcsec rms (i.e. close to the binned pixel size). The deep images were used to extract the sources by means of the SExtractor package (Bertin & Arnouts 1996). The number of sources detected above 3σ are 931 in the centre and 925 in the offset position (after removing several clearly spurious sources appearing on the edges of the detectors). Since there is quite a large overlap between both positions, we found 374 common sources after matching both source catalogues using TOPCAT (Taylor 2005). These common sources were used as a test of the relative consistency of our astrometry: 245 sources (65%) were found within a match radius of 0.5 arcsec (i.e. consistent with the quoted accuracy), 88 (24%) within 0.75 arcsec, and 15 (4%) within 1.0 arsec radius. Twenty-six objects (i.e. 7%) were matched at larger radii (around 1.5 arcsec), but these sources were always found on the edges of the images, where the OSIRIS field suffers a larger distortion.

The catalogue of detections contains 1482 unique sources. For each detected source and scan step, the best possible combination of individual images was computed, defining this as the best combination of TF tune and dither position at the location of the source. In practise, we deemed the "best combination" algorithm as the selection of all the images for which the TF wavelength at the position of the source lies within a range of ±3 Å (i.e. half scan step) of the given one. For each of these combinations, a synthetic equivalent filter transmission profile was derived by adding up the transmission profiles of all the images entering the combination and fitting the result to the function given in Eq. (4). These synthetic profiles allowed us to verify that our combination approach does not introduce a significant error in the wavelength of the central position (less than 1 Å maximum) or in the FWHM (the average equivalent FWHM is 12.7 Å with a deviation of 0.4 Å). The output combined image is used to determine the flux at this specific scan step and

Table 3. Spectrophotometric standard stars.

Name	mag(λ, Å)	Reference	Position
G157–34	15.35(5400)	Filippenko & Greenstein (1984)	offset
G191–B2B	11.9(5556)	Oke (1990)	offset
Ross 640	13.8(5556)	Oke (1974)	centre

source position by means of SExtractor. The resulting "pseudo-spectra" consist of 50 (47) tuples (λ at source position, flux). The FWHM of the equivalents (synthetic) TF Airy transmission profiles derived at each source position and TF tune were also included in each pseudo-spectrum file. A pseudo-spectrum should not be confused with a standard spectrum produced by a dispersive system: the flux at each point of the pseudo-spectrum is what is integrated within a filter passband centred on the wavelength of the point. Mathematically, a pseudo-spectrum is therefore the convolution of the source spectrum with the TF transmission profile.

3.2. Flux calibration

The flux calibration of each TF tune has been carried out in two steps: first, the total efficiency $\epsilon(\lambda)$ of the system (telescope, optics and detector) should be derived and is computed as the ratio of the measured-to-published flux $F_{\rm m}(\lambda)/F_{\rm p}(\lambda)$ for a set of exposures of spectrophotometric standard stars (Table 3) taken in photometric conditions within a range of tunes compatible with the cluster observation (ideally at the same tunes). The fluxes of the standards are measured by aperture photometry, and the exact wavelengths at the positions of the star are derived from Eqs. (2) and (3). The published fluxes are also derived at these wavelengths by means of a polynomial fit to the tabulated fluxes (see references in Table 3). Then, measured fluxes in engineering units (ADU) are converted to physical units (erg s^{-1} cm^{-2} Å^{-1}) using the expression

$$F_{\rm m}(\lambda) = \frac{g\,K(\lambda)\,E_\gamma(\lambda)}{t\,A_{\rm tel}\,\delta\lambda_{\rm e}} F_{\rm ADU}(\lambda) \tag{5}$$

where g is the CCD gain in e$^-$ADU^{-1}, $E_\gamma(\lambda)$ is the energy of a photon in ergs, t the exposure time in seconds, $A_{\rm tel}$ the area of the telescope primary mirror in cm^2, $\delta\lambda_{\rm e}$ the effective passband width[5] in Å, and $K(\lambda)$ the correction for atmospheric extinction,

$$K(\lambda) = 10^{0.4\,k(\lambda)\,\langle\chi\rangle}, \tag{6}$$

which depends on the extinction coefficient $k(\lambda)$ and the mean airmass $\langle\chi\rangle$ of the observations. In our case, we estimated $k(\lambda)$ by fitting the extinction curve of La Palma[6]. in the wavelength range of interest.

The uncertainty in the efficiency was computed by error propagation, taking the errors in the measured fluxes into account (which in turn include terms for coping with the error of the aperture photometry and the uncertainty of the wavelength tune) and those of the published ones.

The efficiency $\epsilon(\lambda)$ (sampled with nine tunes at position A and 19 tunes at position B must then be fitted to an analytical function of λ in order to perform the calibration at the wavelength of each tune and source. In both cases, the best solution has been a constant efficiency for $\lambda \leq 9270$ Å and a linear decreasing dependency at longer wavelengths (Table 4).

Table 4. Efficiencies for Cl0024 observations.

Position	$\lambda \leq 9270$ Å	$\lambda > 9270$ Å	
	$\langle\epsilon\rangle$	Zero point	Slope
Centre	0.1779 ± 0.0236	10.2497 ± 1.2181	-0.0011 ± 0.0001
Offset	0.1993 ± 0.0035	12.8566 ± 0.9074	-0.0014 ± 0.0001

The second step is to convert the measured flux in ADU of each source at each tune i to physical units (erg s^{-1} cm^{-2} Å^{-1}) by means of the expression

$$f(\lambda)_i = \frac{g\,K(\lambda)\,E_\gamma(\lambda)}{t\,A_{\rm tel}\,\delta\lambda_{\rm e}\,\epsilon(\lambda)} f_{{\rm ADU},i}, \tag{7}$$

where $\epsilon(\lambda)$ is the total efficiency computed above and the remaining terms are as in Eq. (5). The flux errors are computed again by propagation, taking the efficiency errors derived above into account, along with the source flux measurement uncertainty computed by the TFRED `tspect` task as

$$\Delta f = \sqrt{A_{\rm pix}\sigma^2 + f/g} \tag{8}$$

where $A_{\rm pix}$ is the measurement aperture area in pixels, σ the standard deviation of the background noise, and g the gain in in e$^-$ADU^{-1}.

3.3. Ancillary data

Within the process of generating the catalogue of line emitters and further data analysis, we have made use of public Cl0024 catalogues[7] from the collaboration "A Wide Field Survey of Two $z = 0.5$ Galaxy Clusters" (Treu et al. 2003; Moran et al. 2005, hereafter M05) that include photometric data for 73 318 sources detected and extracted in the HST WFPC2 sparse mosaic covering 0.5×0.5 deg (Treu et al. 2003) and in ground-based CFHT CFH12k *BVRI* and Palomar WIRC $JK_{\rm s}$ imaging. Visually determined morphological types are given for all sources brighter than $I = 22.5$. In addition, thousands of photometric and spectroscopic redshift estimates are available. The catalogue of spectroscopically confirmed objects within the field (including foreground, cluster, and background sources) comprises 1632 sources (see Moran et al. 2007, and references therein).

4. The catalogue of ELGs

To produce a catalogue of ELGs, we start by selecting the line emitters. The first step to getting the catalogue of ELGs is to select line emitters (either Hα at the redshift of the cluster or with other lines in the case of background contaminants). In many cases, the emission line showed up as very clear, and even in a fraction of the emitters, the Hα and [N II] lines appeared clearly resolved, but given the number of input sources, an automated or semi-automated procedure was required. The TFRED package provides a task, `tscale`, that outputs the putative ELGs from the source catalogue, but when applied to our input catalogue, it did not yield reliable results: it was designed for a reduced number

[5] $\delta\lambda_{\rm e} = \frac{\pi}{2} FWHM_{\rm TF}$.

[6] http://www.ing.iac.es/Astronomy/observing/\manuals/ps/tech_notes/tn031.pdf

[7] http://www.astro.caltech.edu/~smm/clusters/

of scans and sparse spectral sampling, and it frequently failed to classify even the most obvious ELGs from our densely sampled pseudo-spectra. Instead, we followed a different approach by creating an automatic selection tool, implementing the following steps:

(i) Define a "pseudo-continuum" (hereafter referred as pseudoc) as the subset of pseudo-spectrum points resulting from discarding "high/low" outlier values, defined as those above or below the median value $\widetilde{\mathrm{flux}}_{\mathrm{alldata}} \pm 2 \times \sigma_{\mathrm{alldata}}$. The "pseudo-continuum" level, $\mathrm{flux}_{\mathrm{pseudoc}}$, is defined as its median and the "pseudo-continuum" noise, $\sigma_{\mathrm{pseudoc}}$, as its standard deviation.
(ii) The "upper" value is defined as $\mathrm{flux}_{\mathrm{pseudoc}} + 2 \times \sigma_{\mathrm{pseudoc}}$. Then, the criteria for determining a reliable ELG candidate have been defined as A) either two consecutive values above "upper" are found, or B) one point above "upper" is found and, in addition, one contiguous point above $\mathrm{flux}_{\mathrm{pseudoc}} + \sigma_{\mathrm{pseudoc}}$ and one contiguous point above $\mathrm{flux}_{\mathrm{pseudoc}}$. These criteria have been chosen because we observed in our simulations (see below) that even very narrow lines, (0.7 Å) always produce a high positive signal in at least two scan slices around the maximum. Single-point peaks in the pseudo-spectrum are attributed to noise or to artefacts. On the other hand, the criteria above can cope with broad-line AGNs (see Sect. 8).

To investigate the reliability of this automatic classifier, we created several simulated spectra comprising an emission line with a Gaussian profile and a flat continuum (a good approximation within our relatively narrow spectral range). This simple spectrum is convolved with an Airy profile with $FWHM$ = 12 Å and sampled at steps of 6 Å to produce a noiseless pseudo-spectrum. Finally, a noise component is built by drawing random values from a normal distribution with zero mean and by varying standard deviation and adding it to the pseudo-spectrum signal. We have built a collection of 800 such pseudo-spectra by varying different input parameters:

(i) The range of intrinsic line widths of the lines has been adopted from the typical limiting values of the integrated line profiles of giant extragalactic HII regions from Roy et al. (1986), from some 20 km s^{-1} to about 40 km s^{-1}, which corresponds to a range $FWHM_{\mathrm{line}} = 0.7-1.5$ Å (rest frame) with 0.4 Å step; this range has been extended further by one additional step up to 2.3 Å (65 km s^{-1}) in order to cope with blending of several HII regions within the galaxy.
(ii) The range of shifts in the peak of the line with respect to the maximum filter transmission has been set to 0−3 Å with 1 Å step (i.e. consistent with the scan step of 6 Å).
(iii) The equivalent width (EW) of the emission line has been varied in the range 5−15 Å with steps of 1 Å. This range explores our detection sensitivity threshold; at larger EW we do not expect line identification problems.
(iv) Finally, the amplitude (standard deviation) of the added random noise component, σ_{noise}, was set in the range 0.1 to 0.4 times the maximum of the line, with steps of 0.1.

The automatic classifier has identified 726 out of the 800 simulated pseudo-spectra as line emitters (i.e. more than 90%). From those, only in two cases did the classifier choose the source based on a noise feature rather than the correct line. As expected, the 74 pseudo-spectra not classified as ELG are in the high noise range (0.3 or 0.4).

Moreover, to determine the possibility of automatically classifying a passive galaxy as ELG, we generated a set of pseudo-spectra in a similar way based on a flat continuum and σ_{noise} in the range of 0.1 to 0.3 times the continuum flux value, in steps of 0.01. (A finer step was chosen to create enough instances, given that the noise is the only variable parameter.) At each noise step, we generated 21 instances, yielding a total number of 420 pseudo-spectra. From these, 316 (i.e. more than 75%) were classifed as passive, while the remaining 104 (i.e. less than 25%) were classified as ELG.

The results of the simulations indicate that our simple classification algorithm is quite effective at classifying true ELGs as line emitters, but can also pick a non-negligible amount of noisy pseudo-spectra of passive galaxies as emission line objects. Therefore, we have added an additional step, filtering the sample produced by the selection tool by a careful visual inspection of the pseudo-spectra and also of the thumbnails of all scan slices for every source of this output sample (done by three collaborators separately). After applying these two steps, we extracted a sample of 210 very robust (i.e. high S/N) ELGs, comprising both star-forming galaxies and AGNs.

4.1. Line wavelength estimation

Estimating the wavelength of the Hα line is possible with TF tomography, but it is generally a complex issue, since on the one hand, we have a blend of three lines (the Hα line plus the two components of the [N II] doublet), convolved with the transmission profile of the TF, As described in Sect. 5, in many cases the pseudo-spectrum line "profile" (hereafter referred to as line pseudo-profile) is affected by absorption-like features. We attempted to derive the Hα line position by considering a model comprising three Gaussian lines plus a linear continuum. The rest-frame wavelength's relative positions are fixed, as is the ratio of the two [N II] doublet components (set to f_{6548}/f_{6583} = 0.3). Free parameters of the model are the observed wavelength of the Hα line, the line width (constrained to be the same for the three lines), the [N II] λ 6583 and Hα fluxes, and the continuum level. This model spectrum was convolved with the TF transmission profile and fitted by means of non-linear least squares to the pseudo-spectra profiles.

For some 30% of the sources, the result of the fit reproduces the pseudo-spectrum profile accurately, but in a vast majority of the cases, the fit either fails or provides inaccurate results owing to noise in the pseudo-continuum, absorption-like features in the line pseudo-profile, etc. Eventually, we decided to derive the position of the line by manually fitting the pseudo-spectrum using the IRAF `splot` task after inspection and either a Gaussian or a Lorentzian profile, choosing the appropriate range to avoid continuum noise and contaminant lines. There is very good agreement between the line positions computed by `splot` and those resulting from the trustful, accurate model fits (∼1 Å). In a minority of the cases, where the line profile showed very asymmetric (e.g. when absorption-like features are present, most likely from random noise as shown in Sect. 5 below), the position of the line was chosen to be the peak value of the pseudo-spectrum. Given the difficulty of providing a trustful uncertainty figure, we have assumed a constant error value of 3 Å for the fit to the peak of the line, i.e. half of a scan step. This error is square-added to the tuning uncertainty of 1 Å and to the wavelength error introduced by the combination of images used to produce the pseudo-spectrum (see Sect. 3.1), also considered to be 1 Å at most; hence, $\sigma_{\mathrm{pos}} \simeq 3.3$ Å.

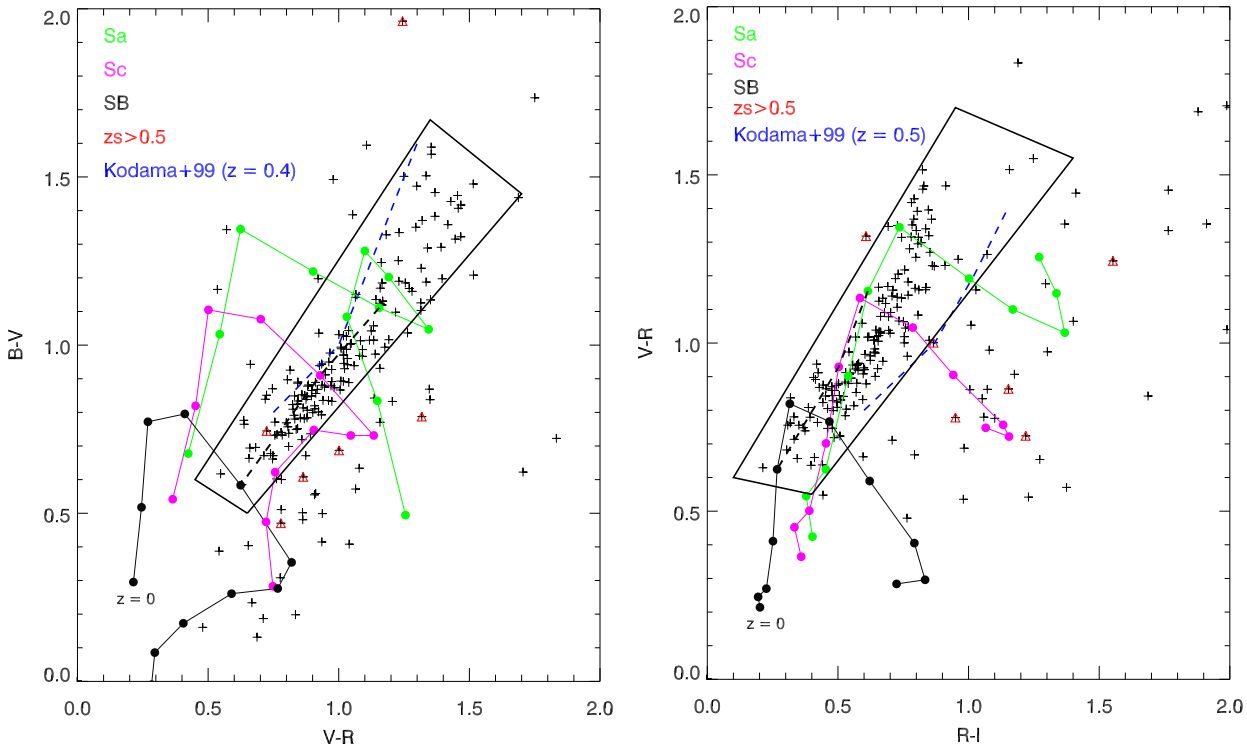

Fig. 2. $B-V$ vs. $V-R$ (*left*) and $V-R$ vs. $R-I$ (*right*) diagnostic diagrams. The sample, comprising 202 unique objects with counterparts in the M05 catalogue is denoted by crosses (+). The red triangles (△) denote objects with spectroscopic redshift $z_s > 0.5$ in the M05 catalogue. The control grid has been built using synthetic colours from COSMOS templates for Sa, Sc, and SB galaxies in the range $z = 0.0$–1.0 with steps of $\Delta z = 0.1$. The thick black dashed line connects the three templates at $z = 0.4$. The blue dashed line depicts the Kodama et al. (1999) models at $z = 0.4$ and $z = 0.5$. The thick black solid line box marks the approximate region used for selecting the cluster candidates.

4.2. Identification of Hα emitters: rejection of interlopers

The observations presented here target a single emission line, so several interlopers can be present, and they are expected to be ELGs at other redshifts. When observing Hα at $z = 0.40$, [O III]λ 5007 Å emitters at $z = 0.83$ and [O II]λ 3727 Å emitters at $z = 1.46$ can be detected as well. However, at the limiting fluxes considered here, these contaminants are not expected to be very abundant and can be easily distinguished via colour−colour diagrams. We implemented these colour−colour diagnostic diagrams following Kodama et al. (2004) according to the following steps: first, we matched our initial catalogue of 210 robust candidates to the photometric and spectroscopic catalogue from M05 and a matching radius of 1.0 arcsec (i.e. compatible with the accuracy of our astrometry).

A counterpart with at least photometric data was found for 202 sources. Using the CFHT CFH12k aperture photometry, we computed the $B-V$, $V-R$, and $R-I$ colours. The diagnosis grid was built by deriving synthetic colours for COSMOS templates Ilbert et al. (2009) of Sa, Sc, and starburst (SB) galaxies at redshifts ranging from $z = 0$ to $z = 1.0$ in steps of 0.1, integrated to the CFH12k B, V, R, and I passbands. Also, models from from Kodama et al. (1999) at $z = 0.4$ and $z = 0.5$ have been included in the grid. The diagrams for $B-V$ vs. $V-R$ and $V-R$ vs. $R-I$ are shown in Fig. 2. A source has been deemed to be an interloper if (i) the source is outside the cluster region (as depicted in Fig. 2) in both colour diagrams and does not have a spectroscopic redshift from M05 within the cluster range (set as $0.35 \leq z \leq 0.45$); and (ii) the source has a spectroscopic redshift from M05 outside the cluster range, independent of its colours.

Based on the first criterion, we have deemed 19 sources as contaminants. In a vast majority of the cases, these are located in the locus of the colour−colour diagram occupied by galaxies at $z = 0.8$–1.0, i.e. consistent with being [O III]λ 5007 Å emitters. Moreover, 97% of the ELGs with a redshift from M05 within the cluster range were also catalogued as cluster members by the colour-colour diagnostic described above. The second criterion added nine additional sources as interlopers. (Two sources were discarded by both colours and redshift criteria.) As a result, 28 objects were classified as contaminants at a different redshift. In addition, eight sources do not have any counterpart in the M05 catalogue and therefore have been excluded from the cluster list. Therefore, our final catalogue consists of 174 robust cluster Hα emitters (see the distribution of sources in the sky in Fig. 4), 28 putative interlopers (ELGs at a different redshift, mostly oxygen emitters at $z \sim 0.9$), and 8 sources without ancillary data to perform the assessment. Future analysis of additional spectral ranges (centred on the [O III] and Hβ wavelengths at the nominal redshift of Cl0024) will refine this rejection criterion. The 174 sources in our final catalogue of unique robust cluster emitters are listed in Table 5. From these, 112 have spectroscopic redshifts in the M05 catalogue.

Figure 3 shows a selection of high signal-to-noise pseudo-spectra. In many cases, the strongest [N II] doublet component (at 6583 Å) is clearly separated from the Hα line in a visual inspection. Sometimes the line is observed as a "shoulder" on the long wavelength side of the Hα line.

5. Derivation of line fluxes

From the pseudo-spectra described in Sect. 4, it is possible to derive the Hα and [N II] fluxes following several approaches. We applied a straightforward procedure derived from the standard

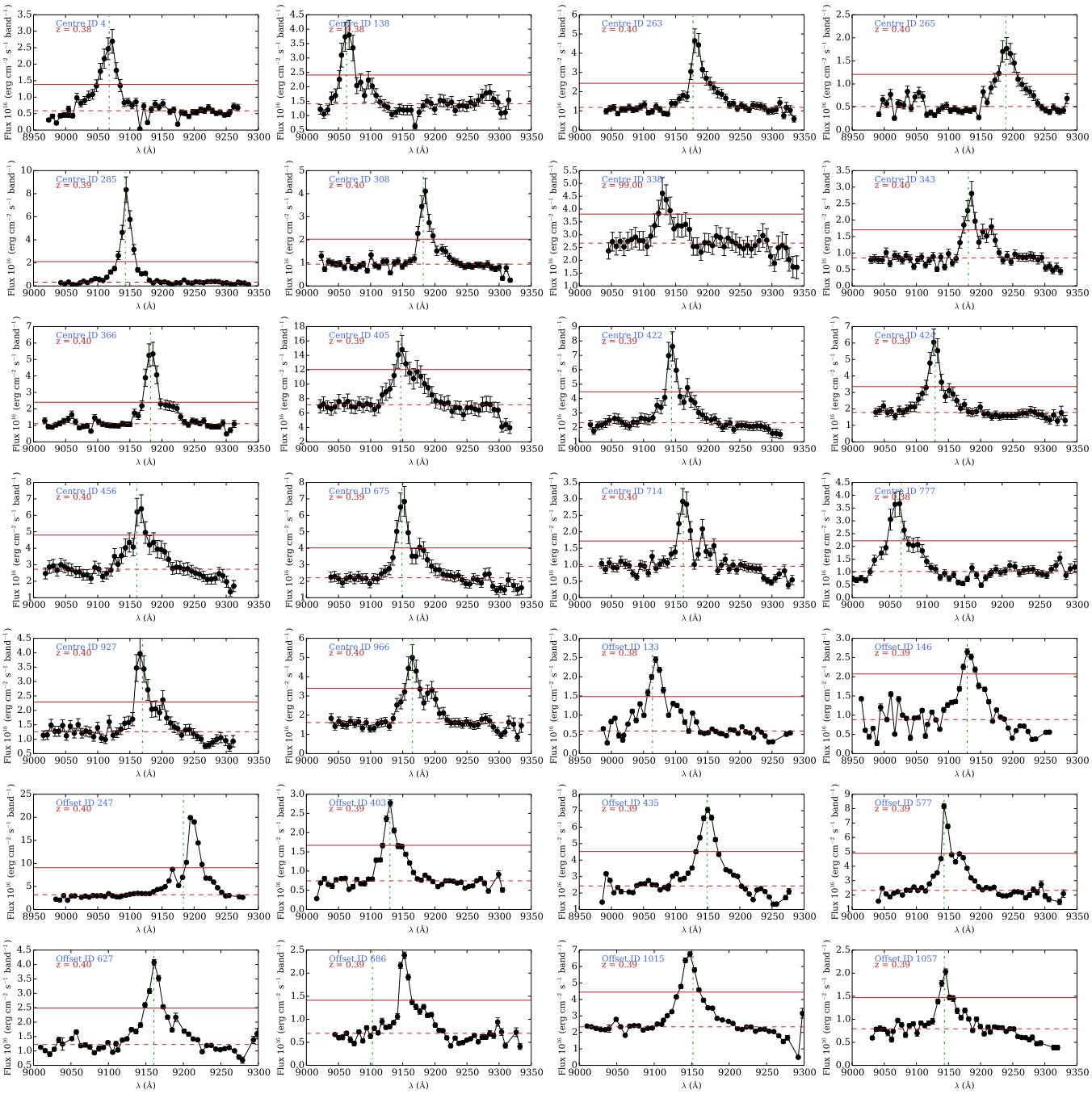

Fig. 3. Selection of 28 pseudo-spectra with high S/N. The green dashed-dotted lines correspond to spectroscopic or secure photometric redshifts from M05 (when available). The dashed red line corresponds to the approximate pseudo-spectrum continuum level, and the solid red line to the $3\sigma_{\rm cont}$ level, where $\sigma_{\rm cont}$ is the pseudo-continuum noise. For the source ID offset/686, the redshift from M05 is photometric.

narrow-band on-band/off-band technique, using for each source the flux in the scan slice closest to the computed position of the Hα line (see Sect. 4) and that of the slice closest to the [N II] line. As is shown below, this method, though simple, produces acceptable results when compared to the more sophisticated procedure based on least-squares fitting of the pseudo-spectrum to a model spectrum convolved with the transmission profile of the TF described in Sect. 4.1 with the advantage that the former method is always applicable, while the latter can only be used in a minority of cases.

We start by subtracting a linear continuum. This can be done easily by applying a linear fit to the regions of the pseudo-spectrum excluding the emission line. Then, assuming infinitely thin lines, the Hα and [N II] line fluxes, denoted by f (Hα) and f ([N II]) respectively, are given by the expressions (Cepa, priv. comm.):

$$\begin{aligned} f_{\rm on,H\alpha} &= T_{\rm H\alpha}\,({\rm H}\alpha)\, f\,({\rm H}\alpha) + T_{\rm H\alpha}\,([{\rm N\,II}])\, f\,([{\rm N\,II}]) \\ f_{\rm on,[N\,II]} &= T_{\rm [N\,II]}\,({\rm H}\alpha)\, f\,({\rm H}\alpha) + T_{\rm [N\,II]}\,([{\rm N\,II}])\, f\,([{\rm N\,II}]) \end{aligned} \quad (9)$$

where $f_{\rm on,H\alpha}$ and $f_{\rm on,[N\,II]}$ are the continuum-subtracted fluxes in the chosen Hα and [N II] slices, and $T_{\langle{\rm slice}\rangle}\,(\langle{\rm line}\rangle)$ denotes the TF transmission of a given slice at a given line wavelength. The different transmission values can be easily derived from the

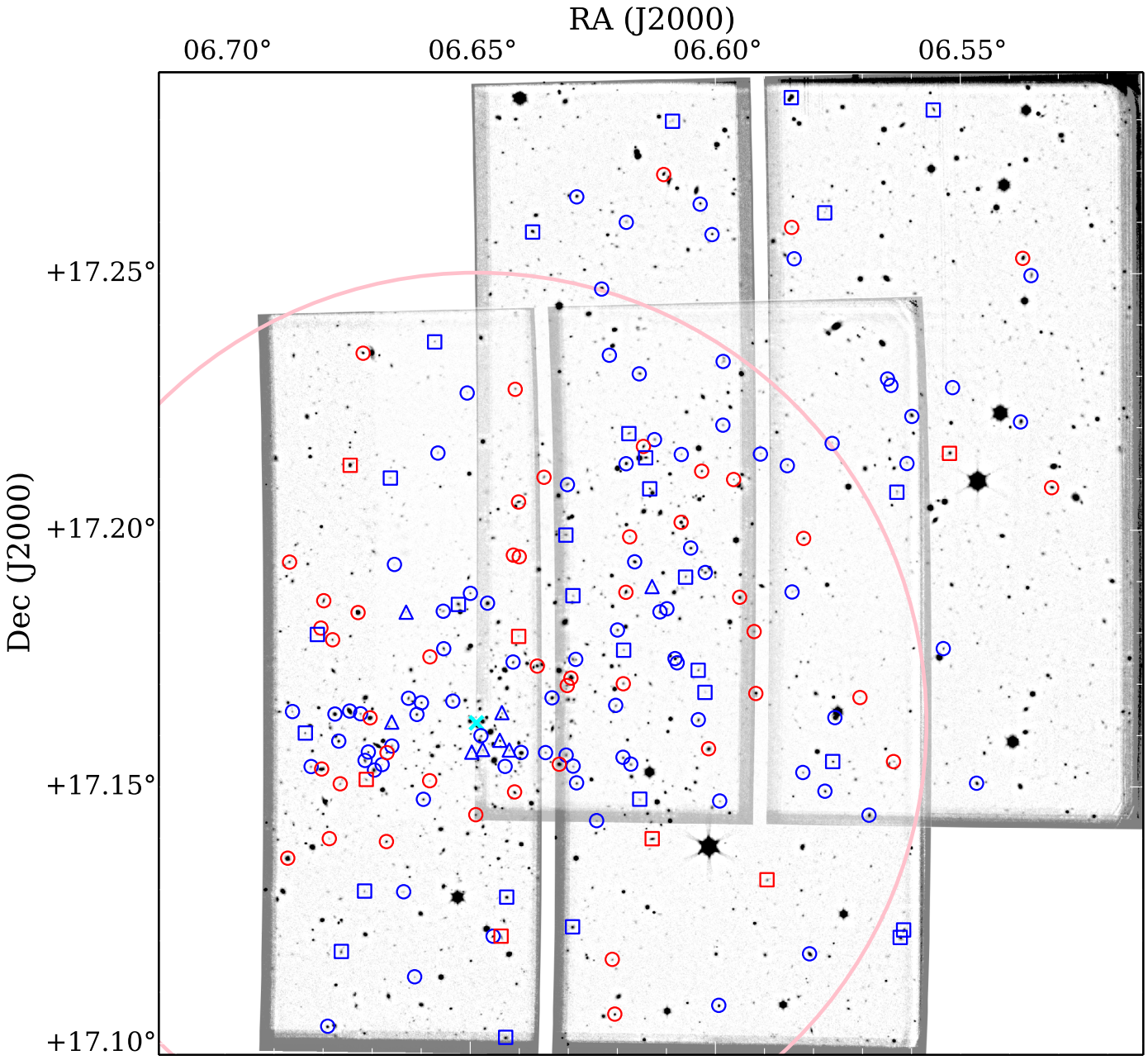

Fig. 4. Two OSIRIS/GTC pointings towards Cl0024. The plot has standard orientation: north is at the top and east to the left. Blue symbols correspond to SF galaxies and red ones correspond to AGNs according to the [N II]/H$\alpha \geq 0.6$ criterion from Ho et al. (1997). Circles correspond to galaxies in the main cluster structure (structure "A" in Sect. 6), squares to those in the infalling group (structure "B"), and triangles to sources in the putative group around $z \approx 0.42$ (see Sect. 6). The cyan cross (×) denotes the centre of the cluster (galaxies/BCG) and the large pink circle denotes the virial radius of 1.7 Mpc (Treu et al. 2003). A general alignment of ELGs is observed in the NW SE direction, consistent with a a structure assembling onto the cluster core from the NW with an orientation almost in the plane of the sky (Moran et al. 2007; Zhang et al. 2005; Kneib et al. 2003).

approximate expression given in Eq. (4). From Eq. (9) we can easily derive the flux in the Hα line:

$$f\,(\mathrm{H}\alpha) = \frac{f_{\mathrm{on,H}\alpha}\,T_{[\mathrm{N\,II}]}\,([\mathrm{N\,II}]) - f_{\mathrm{on,[N\,II]}}\,T_{\mathrm{H}\alpha}\,([\mathrm{N\,II}])}{T_{\mathrm{H}\alpha}\,(\mathrm{H}\alpha)\,T_{[\mathrm{N\,II}]}\,([\mathrm{N\,II}]) - T_{\mathrm{H}\alpha}\,([\mathrm{N\,II}])\,T_{[\mathrm{N\,II}]}\,(\mathrm{H}\alpha)} \quad (10)$$

and a similar expression for the [N II] line. The errors in the lines have been derived by propagation, taking not only the errors in the Hα and [N II] "on" bands, but also the continuum noise into account (i.e. the noise around the zero-level continuum after removing the linear fit explained above). As a result, the line error has been computed as

$$\begin{aligned}\Delta f\,(\mathrm{H}\alpha) = {} & (\,(T_{[\mathrm{N\,II}]}\,([\mathrm{N\,II}])\,\Delta f_{\mathrm{on,H}\alpha})^2 \\ & + (T_{\mathrm{H}\alpha}\,([\mathrm{N\,II}])\,\Delta f_{\mathrm{on,[N\,II]}})^2\,) \\ & + ((T_{[\mathrm{N\,II}]}\,([\mathrm{N\,II}]) - T_{\mathrm{H}\alpha}\,([\mathrm{N\,II}]))\,\sigma_{\mathrm{cont}})^2)^{1/2} \\ & / (T_{\mathrm{H}\alpha}\,(H\alpha)\,T_{[\mathrm{N\,II}]}\,([\mathrm{N\,II}]) - T_{H\alpha}\,([\mathrm{N\,II}])\,T_{[\mathrm{N\,II}]}\,(H\alpha))\end{aligned} \quad (11)$$

where $\Delta f_{\mathrm{on,H}\alpha}$ and $\Delta f_{\mathrm{on,[N\,II]}}$ are the flux errors in the "on" Hα and [N II] bands computed as indicated in Sect. 3.2 and σ_{cont} is the continuum error measured as the standard deviation of the points within the region of the pseudo-spectrum excluding the

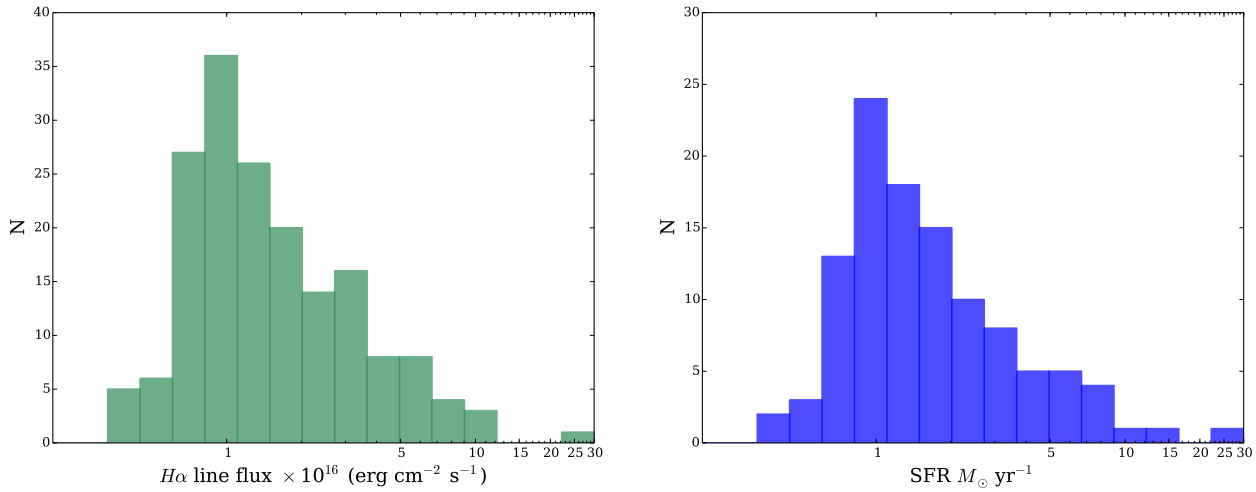

Fig. 5. *Left*: histogram of Hα line fluxes for the 174 robust cluster members (after correcting for the strongest component of the [N II] doublet). *Right*: histogram of SFR for SF galaxies (i.e. excluding AGN candidates) from the Hα fluxes, when applying a standard 1 mag. extinction correction for the line, and the Kennicutt (1998) luminosity-SFR conversion.

emission lines. The contribution of the continuum noise to the total error is important, on average ∼30% at the central position and much greater at the offset position where the exposure times are shorter, on average 60–70%.

The median fractional error in the Hα fluxes is ≈24%. Seventy percent of the sample objects have relative errors below 30%. These errors are compatible with those quoted by Lara-López et al. (2010) (see Sect. 2.2), though somewhat larger than those derived from their simulations due to our larger continuum errors. However, since the [N II] line is usually fainter than the Hα line, its flux errors are in general much greater: the average fractional error is ≈54%, and only 15% of the sample objects have a relative error below 30%. This was, of course, expected since the detection/selection algorithm is driven by the strongest line present in the pseudo-spectrum. In many cases, therefore, the Hα line acts as a "prior", and the nitrogen flux is extracted at the expected wavelength of the (otherwise barely detected) [N II] line.

As mentioned above, the line flux estimation is based on an infinitely thin line approximation that assumes that the line can be represented well by $\delta(\lambda - \lambda_z)$, where $\lambda_z = \lambda_0(1+z)$. According to Pascual et al. (2007), for star-forming galaxies, emission line widths are mass-related and typically $FWHM \lesssim 10\,\text{Å} \times (1+z)$, and for narrow-band filters of some 50 Å width, it is possible to recover ∼80% of the line flux up to $z \sim 4$. We investigated the impact of applying such an approximation to our very narrow TF scans (∼12 Å).

To this end, we performed several simulations using Gaussian line profiles of several widths peaking at different offsets with respect to the maximum of the filter transmission profile (Eq. (4)). The emission line broadening is given by the relation (Fernández Lorenzo et al. 2009):

$$2V_{\max} = \frac{\Delta\lambda c}{\lambda_0 \sin(i)(1+z)} \tag{12}$$

where $V_{\max}$ is the maximum rotation velocity, λ_0 the line wavelength at $z = 0$, and $\Delta\lambda$ the line width at 20% of peak intensity. For a Gaussian line, $\Delta\lambda = 1.524 \times FWHM$. Assuming $V_{\max} = 200\,\text{km s}^{-1}$ as a safe upper limit (see, for instance, Fernández Lorenzo et al. 2009), the Hα line $FWHM \simeq 8$ Å. Here we assume that the line is unresolved. The possibility that the line appears resolved in our pseudo-spectra due to kinematical split is investigated below. For narrow lines, $FWHM = 2$ Å, we are able to recover 96% to 98% of the flux (from 0 to 2 Å offset), while for the widest simulated lines, $FWHM = 8$ Å, the fraction of recovered flux is in the range 73% to 76%.

To compare the simulations with real results, we used the small set of pseudo-spectra for which a reliable fit to the model spectrum was achieved, finding that the average ratio between the flux derived from the infinitely thin line approximation and the one derived from the best fit is 0.81 and 0.88 for the Hα and [N II] lines, respectively, hence well aligned with the results of our simulations. The completeness limit of the ELG sample, as given by the maximum of the flux histogram depicted in Fig. 5 (left panel), is $\sim 0.9 \times 10^{-16}$ erg s^{-1} cm^{-2}, which is better than the GLACE requirements.

5.1. Absorption-like features in the pseudo-spectra

In a large number of cases, we observed absorption-like features that affect the (putative) Hα emission line in the pseudo-spectra. This affects around 50% of the galaxies and is very clear in about 25% of the cases, such as those depicted in Fig. 6. We have explored several possible explanations: first and perhaps most obvious is that the absorption-like features are due to random noise. These characteristics have been observed in the simulations described in the preceding sections, in approximately 20% of the cases (some 146 out of 726 simulated pseudo-spectra classified as ELGs). This is therefore a very probable explanation in an ample portion of the cases. In addition, we explored two potential physical explanations: either an emission line split due to the galaxy rotation or the presence of underlying stellar absorption.

To investigate the first possible cause, we performed a series of simulations similar to those described in the preceding section but starting with a spectrum comprising two identical Gaussian lines with separation $2\lambda_0(1+z)V_{\max}/c$ and a flat continuum in order to re-create the effect of the rotational split in TF pseudo-spectra. We built our collection of pseudo-spectra by varying the range of intrinsic line widths in the range $FWHM_{\text{line}} = 0.7$–2.3 Å (rest frame) with 0.4 Å step; the range of shifts of the peak of the line with respect to the maximum filter transmission was set to 0–3 Å with 1 Å step, and finally the galaxy rotational

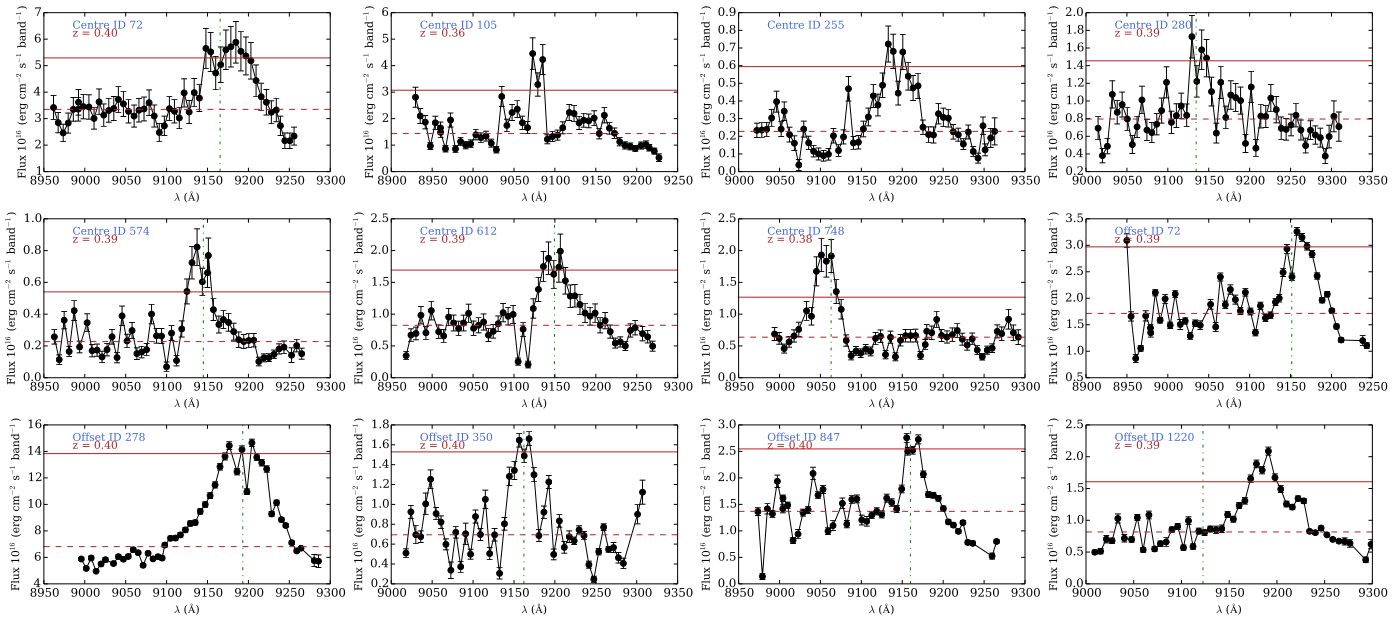

Fig. 6. Selection of pseudo-spectra with a variety of absorption-like features. Lines as in Fig. 3. For the source ID offset/1220, the redshift from M05 is photometric.

speed was let to vary in the range $V_{\rm max}$ = 100–200 km s^{-1} with 10 km s^{-1} step, in agreement with Fernández Lorenzo et al. (2009). As a result, the separation between the two line peaks ranges from some 6.1 Å to about 12.3 Å; and finally the amplitude of the added random noise component ($\sigma_{\rm noise}$) was set in the range 0.1 to 0.3 times the maximum of the line in steps of 0.1.

After inspecting 1320 pseudo-spectra simulated as described above, we observed that the number of absorption-like features observed in the pseudo-spectra is relatively low at rotational speeds ≤160 km s^{-1}, ranging from approximately 10% at 100 km s^{-1} to some 26% at 160 km s^{-1}, hence consistent with noise-induced features. However, the fraction of features observed raises notably for $V_{\rm max} \geq$ 170 km s^{-1}, which is 45% at 170 km s^{-1} and 58%–60% above that speed. Therefore, a kinematical line split due to galaxy rotation is a plausible mechanism to induce a fraction of the absorption-like features observed. Nevertheless, it should be taken into account that the fraction of such fast-rotating galaxies is reduced (around 14% in the sample of Fernández Lorenzo et al. 2009, in the range $0.3 < z < 0.8$) and, moreover, that we are assuming $\sin i = 1$, i.e. edge-on or nearly edge-on galaxies so the actual fraction of objects fulfilling the conditions is probably of the order of 14% at most.

We finally explored the possibility that these absorption-like features are caused by true absorption due to the underlying host galaxy stellar component. To this end, the most likely host galaxy stellar population was derived by fitting the public photometric information from M05 (B, V, R, I from CFHT; J, $K_{\rm s}$ from WIRC at Palomar 200″) by means of the *LePhare* code (Ilbert et al. 2006) using the set of SED templates from Bruzual & Charlot (2003), SF histories exponentially declining with time as $SFR \propto {\rm e}^{-t/\tau}$ with τ ranging from 0.1 to 30.0 Gyr, initial mass function (IMF) from Chabrier (2003), and dust extinction law from Calzetti et al. (2000). The details of the computations will be thoroughly described in Pérez-Martínez et al. (in prep.).

The best-fitting host galaxy stellar template was furthermore sampled again at a finer resolution using GALAXEV[8] (Bruzual & Charlot 2003) and then convolved with the TF transmission profile to obtain a "host galaxy stellar component" pseudo-spectrum. The pseudo-continuum of this synthetic pseudo-spectrum was then scaled to that of the real object within the range of the observations. In some cases, the absorption features were still present in the synthetic pseudo-spectrum and could account for at least a fraction of the absorption-like feature observed. However, owing to the nature of the procedure, the best fit stellar template solution is notably degenerate when taking the photometric errors into account, making the flux correction is uncertain. We therefore decided to omit this correction for the Hα/[N II] line fluxes.

6. Spatial and redshift distribution of the cluster galaxies

Spectroscopic redshifts from M05 were available for 112 of our ELGs (see Sect. 4.2). In all cases, the M05 redshifts also placed our cluster candidates within the cluster. There was a remarkably good agreement between the redshift estimates derived from the position of the Hα line within our pseudo-spectra (see line positions derived from spectroscopic redshifts in Fig. 3) and the one derived from spectroscopic measurements. In fact, the redshift error defined as $|z_{\rm TF} - z_{\rm spec}|/(1 + z_{\rm spec})$ is on average 0.002 (median value 0.0005) with a maximum value of 0.02; i.e., we can consider the TF-derived redshifts as of spectroscopic quality.

The spatial distribution of the ELG sample, as given by the position of the sources in the sky plane and our redshift estimates, maps the presence of two components: (i) a structure assembling onto the cluster core from the NW with an orientation almost on the plane of the sky (already reported by other authors; (Moran et al. 2007; Zhang et al. 2005; Kneib et al. 2003); (ii) an infalling group at high velocity nearly along the line of sight to the cluster centre, which is identified by a double-peaked distribution in the redshift space, as shown in Fig. 7 (Moran et al. 2007; Czoske et al. 2002). Structures "A" (centred at z = 0.395) and "B" (centred at z = 0.381) correspond to the main cluster and infalling group components, respectively.

[8] http://www2.iap.fr/users/charlot/bc2003/

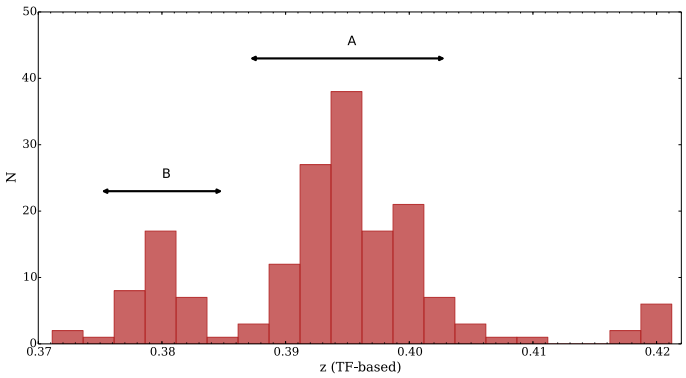

Fig. 7. Distribution of redshifts derived from our data. It is possible to recognize two dynamical structures as in Czoske et al. (2002): "A" is the main cluster component, while "B" lies along the line of sight to the cluster centre and has been interpreted as an infalling group at high velocity.

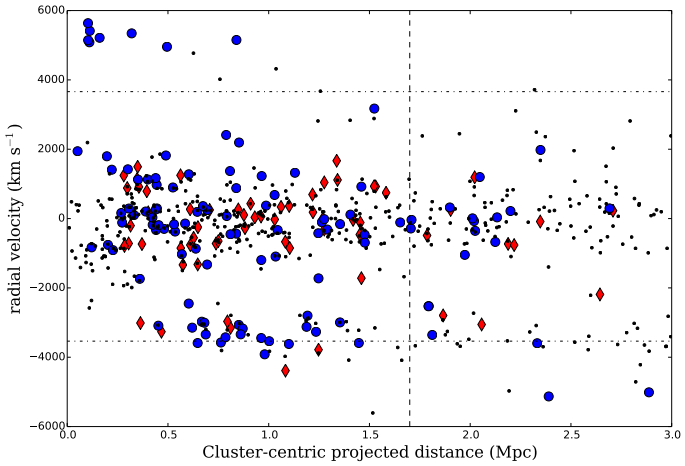

Fig. 8. Line-of-sight velocity relative to the cluster main component central redshift $z = 0.395$ plotted against the projected distance to the cluster centre (as defined by the distribution of galaxies/BCG). Red diamonds correspond to AGNs and blue dots to SF galaxies according to the H97 criterion (see Sect. 8). The dotted vertical line marks the virial radius of 1.7 Mpc (Treu et al. 2003). The dashed-dotted horizontal lines correspond to the radial velocity limits fully covered within the field of view of both OSIRIS TF pointings (see Sect. 3 and Eq. (2)). The small black points correspond to galaxies from M05 with spectroscopic redshifts, including both passive and star-forming objects.

The distribution of galaxies can also be seen in Fig. 8, where the radial velocities relative to the central redshift of component "A" are plotted against the distance to the cluster centre as given by the distribution of galaxies/BGC (Treu et al. 2003). The two mentioned components are clearly separated. There is a third small group of eight galaxies at $z \approx 0.41-0.42$ (clearly seen in Figs. 8 and 7) that has been also reported by Czoske et al. (2002). While according to these authors, these galaxies are most likely part of the surrounding field galaxy population, we cannot rule out the possibility of another group connected to Cl0024. This suggestion could be reinforced by the fact that all these galaxies are observed within a relatively short cluster-centric projected distance, $r < 1$ Mpc. While this can be just an instrumental effect, as a result of the incomplete wavelength coverage on the red side of the velocity field, it should be taken into account that, on the one hand, the cluster centre is offset some 1 arcmin to the SE of the TF axis of the central pointing, and on the other, that no other excess of ELG is observed close to the TF axis of the offset pointing, as would be expected if the galaxies were part of the field galaxy population.

7. Hα + [N II] luminosity function

To verify the accuracy and performance of our photometry, we built the Hα + [N II] luminosity functions computed from sources within a central area of 0.8 Mpc and within $r_{\rm vir} = 1.7$ Mpc. These are depicted in Fig. 9. These cumulative functions can be compared with those of Kodama et al. (2004; hereafter K04). However, while the comparison is direct at the smaller radius, at the larger one we need to consider that the coverage of our observations within $r_{\rm vir}$ is incomplete towards the E and the SE, around 81% of the full circle of $r_{\rm vir}$. We performed a simple area correction to account for this, shown in the right-hand panel of Fig. 9. The completeness of our sample, as measured by the peak of the luminosity histogram, is $\log L(\mathrm{H}\alpha{+}[\mathrm{N\,II}]) \simeq 41$, so very similar to that of K04.

An evident discrepancy between our data set and that of K04 is found at the high-luminosity end, $\log L(\mathrm{H}\alpha{+}[\mathrm{N\,II}]) \gtrsim 41.8$. This is observed not only in the larger area but also in the smaller one, so it cannot be attributed to our incomplete area coverage. However, it should be taken into account that K04 results are based on a different technique, namely a standard narrow-band filter (the Subaru/Suprime-Cam NB_{912} filter with $\lambda_{\rm eff} = 9139$ Å and $FWHM = 134$ Å) plus broad-band BRz' filters meaning that discrepancies in individual objects can be expected. Of course, this only affects a few objects (just 4 objects down to $\log L(\mathrm{H}\alpha{+}[\mathrm{N\,II}]) \simeq 41.8$). At lower luminosities and even beyond the completeness limit, the agreement between our cumulative number counts and those of K04 is excellent, reinforcing confidence in the accuracy of our photometry.

8. Star-forming galaxies and the AGN population

We have explored the available mechanisms for separating the population of SF galaxies and AGNs. Broad-line AGNs (BLAGN) show permitted lines with widths of thousands of kilometres per second. By contrast, in narrow-line AGNs (NLAGN), spectra line Doppler widths are much smaller, typically only a few hundred kilometres per second, which is comparable to or somewhat larger than stellar velocity dispersions. We verified that the profiles of broad lines are reproduced well in our data by simulating BLAGN pseudo-spectra built from real spectra of local universe Seyfert 1 (3C 120, García-Lorenzo et al. 2005) and Seyfert 1.5 galaxies (NGC 3516, Arribas et al. 1997; NGC 4151, Kaspi et al. 1996), which were displaced to the redshift of Cl0024 and convolved with the TF transmission profile (Eq. (4)). Finally, noise components built by drawing random values from a normal distribution with zero mean and a standard deviation equal to 10% of the difference between the peak of the pseudo-spectrum and its median value were added to the pseudo-spectra signal. In all generated instances of such pseudo-spectra, the broad component of the Hα line was clearly traced as depicted in Fig. 10.

To select candidates to BLAGN, we performed simple Gaussian fits to the pseudo-spectra, setting a low line width threshold of $FWHM = 36$ Å (6 scan steps) that is approximately 1180 km s^{-1} at the redshift of Cl0024. The results of the fitting process were carefully inspected, rejecting incorrect or unclear cases (e.g. when two narrow lines were fitted as a single, broad one), arriving at a final list of 25 robust candidates, i.e. 14% of the sample of ELG. Some cases are depicted in Fig. 10.

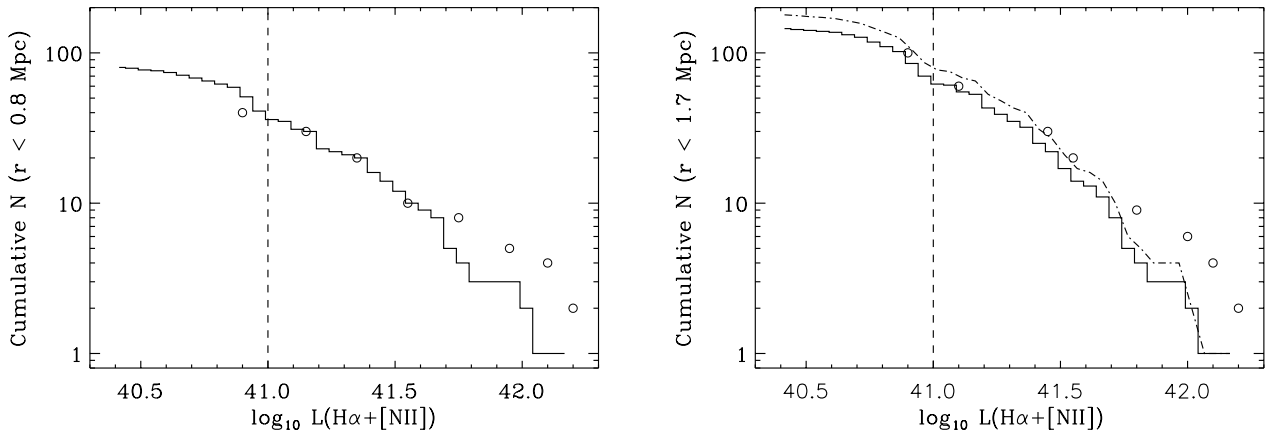

Fig. 9. Cumulative luminosity function (LF) within a radius of 0.8 Mpc (*left*) and $r_{vir} = 1.7$ Mpc (*right*). The solid line corresponds to our galaxy counts, and the big open circles are sparsely sampled points from the Kodama et al. (2004) LF. The dotted-dashed line in the right plot corresponds to our LF corrected for the incomplete area coverage within r_{vir}. The dashed line corresponds to the completeness limit of our data, $\log L(\mathrm{H}\alpha+[\mathrm{N\,II}]) \simeq 41$.

In a second step, we separated NLAGNs from SF galaxies using the ratio between the [N II] and the Hα lines. Moreover, following Cid Fernandes et al. (2010), we combined this ratio with the EW of Hα ($W_{\mathrm{H}\alpha}$) in order to break the degeneracy between Seyfert and LINER galaxies, the so-called "EWαn2 diagram" as depicted in the left-hand panel of Fig. 11. The use of $W_{\mathrm{H}\alpha}$ is justified by the known fact that Seyfert galaxies tend to have a higher power for the ionising engine than for the optical output of the host stellar population. According to Cid Fernandes et al. (2010), a reasonable Seyfert/LINER boundary can be set to $W_{\mathrm{H}\alpha} = 6$ Å. On the other hand, the percentage of NLAGN depends on the limits set to [N II]/Hα. Different criteria have been proposed: Ho et al. (1997; hereafter H97) adopted the classical criterion from Veilleux & Osterbrock (1987) and considered star-forming galaxies, such as those with [N II]/H$\alpha < 0.6$ and NLAGNs in the region [N II]/H$\alpha \geq 0.6$. This region is populated by objects showing pure AGN spectral features (either Seyferts or LINERS) and "transition" or "composite" objects, interpreted as galaxies whose integrated spectra is the superposition of AGN and SF features. The criterion from Kewley et al. (2001; K01) is widely used to separate "pure AGNs" ($\log([\mathrm{N\,II}]/\mathrm{H}\alpha) \geq -0.10$) from SF and composite objects, while those of Kauffmann et al. (2003; K03) and Stasińska et al. (2006; S06) are used to separate "pure SF" galaxies from any AGN or composite object. In Table 6 the percentages of NLAGNs found within our sample are shown after applying the different criteria explained above. Taking the number of BLAGNs found above into account, the total percentage of AGNs with respect to the ELG population ranges from 26% to 54% depending on the diagnostic used. Unless otherwise stated, the H97 criterion will be used hereafter to separate SF and NLAGN classes. According to this criterion, the ratio of BLAGNs with respect to NLAGNs is 64%, so very similar to the ratio of Seyfert 1/Seyfert 2 in the local universe from Ho et al. (1997, 61%) and Sorrentino et al. (2006, 60%) and of (BLAGN+NLAGN)/ELG ~ 37/%.

Regarding the AGN class, all the objects are very likely Seyfert galaxies ($W_{\mathrm{H}\alpha} > 6$ Å). No clear LINER-class objects are detected owing to our EW detection limits.

A cautionary note regarding errors in our estimates: owing to the large uncertainties quoted for the [N II] line fluxes, the errors of the [N II]/Hα ratios are also generally large; in fact, only 30% of the sample has relative errors below 50%, and the vast majority of these objects are AGNs and composite objects. Very large fractional errors in the [N II]/Hα ratios tend to be found in objects where the [N II] line is barely detected, and are thus very likely pure SF galaxies. We therefore eventually decided to keep all sources in the study, regardless of their error in the [N II]/Hα ratio.

Table 6. Percentage of NLAGNs in Cl0024 when applying different criteria.

Criterion	[N II]/Hα	NLAGN number	NLAGN Fraction (%)
"Pure AGN" (K01)	≥0.794	21	12
"Classical AGN" (H97)	≥0.60	39	22
AGN+composite (K03)	≥0.478	60	34
AGN+composite (S06)	≥0.398	69	40

The relative numbers of AGNs with respect to the total number of ELGs obtained in this study are higher than our previous estimates for this cluster (~20%; Pérez-Martínez et al. 2013, only considering NLAGN), but smaller than those obtained by Lemaux et al. (2010) from [O II] and Hα measurements in two clusters at a higher redshift, RXJ1821.6+6827at $z \approx 0.82$ and Cl1604 at $z \approx 0.9$. These authors found that a percentage as large as ~68% of the objects can be classified as AGNs (Seyfert/LINER, using H97 boundaries) and that nearly half of the sample have [O II] to Hα EW ratios higher than unity, the typical value observed for star-forming galaxies. The portion of galaxies classified as AGN in their study was reduced to about 33% for blue galaxies. It is worth mentioning that the results from these authors are derived from a relatively small sample, 19 galaxies (out of a larger sample of 131 [O II] emitters) compared with ours (174 objects).

Furthermore, we have compared our result with the fraction of AGNs, computed with respect to the total number of cluster members brighter than a certain magnitude threshold, obtained by Martini et al. (2002) from a deep X-ray *Chandra* observation of the closer, massive cluster A2104 at $z = 0.154$. They found six sources associated with red galaxies within the cluster whose X-ray properties are compatible with being AGN. Notably, only one of them shows optical features of an active nucleus. The authors conclude that at least $\gtrsim$5% of the cluster galaxies with $R < 20$ (the limiting magnitude of their counterparts) harbour an AGN. To perform a rough comparison, we have

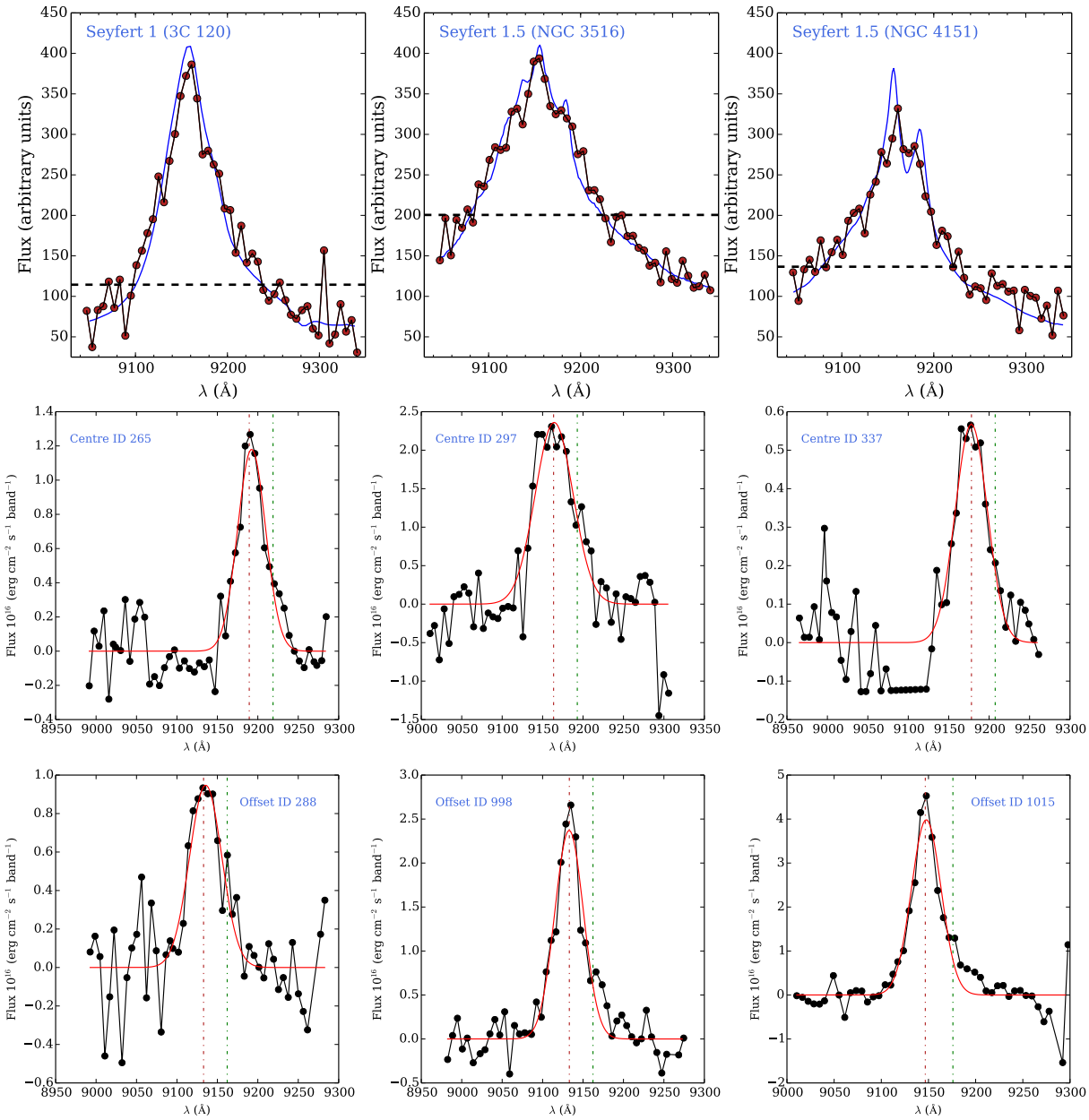

Fig. 10. *Top row*: real spectra of local universe BLAGNs red-shifted to $z = 0.395$ (blue solid line) and instances of the simulated pseudo-spectra (red dots and black continuum line). The dashed horizontal line denotes the median value of the pseudo-spectra. See text for details. *Middle and bottom rows*: actual pseudo-spectra classified as BLAGN. The red and green vertical dash-dotted lines mark the positions of the Hα and [N II] lines, respectively. The red solid line corresponds to the best fit to a Gaussian profile.

determined the R-band magnitude distribution of our AGN sample using M05 broadband data. The limiting magnitude of the Martini et al. (2002) counterparts corresponds to $R = 22.3$ at the redshift of Cl0024. This value corresponds almost exactly to the peak of the R-band magnitude distribution of our AGNs. Within our sample, 45 AGNs have $R \leq 22.3$. We have determined the number of galaxies in the M05 catalogue with $R \leq 22.3$ in the redshift interval $0.35 < z < 0.45$ (both spectroscopic and photometric) within the same area of our AGN sample, obtaining 263 sources. A crude estimate of the fraction of AGNs within our sample would therefore be $45/263 \approx 17\%$, i.e. more than three times greater than the fractions obtained by means of X-ray estimates. However, once again it must be noticed that the X-ray sample is much smaller (and shallower) than ours, and so the result should be considered with care. Actually our percentage of AGNs is similar to the one obtained by Lemaux et al. (2010), 20% at $z \approx 0.9$. This suggests a lack of redshift evolution of the population of faint AGNs in the range $0.4 \lesssim z \lesssim 0.9$, or at least much milder than predicted by Martini et al. (2009) for luminous AGNs, $f \sim (1+z)^{5.3}$.

The average of our AGN luminosity distribution (with no extinction correction) is $\log L(\mathrm{H}\alpha) \simeq 41.0$. At the bright end, we found one AGN with $\log L(\mathrm{H}\alpha) \simeq 41.7$, which corresponds to $\log L_\mathrm{X} \sim 43$ using the $L(\mathrm{H}\alpha)$ to L_X relation from Ho et al. (2001). This detection is compatible with the results from Martini et al. (2009) in the $0.3 < z < 0.6$ bin (four AGNs in ten clusters with $\log L_\mathrm{X} \geq 43$).

We cross-matched our ELG catalogue with a list of source detection positions from a *Chandra* ACIS-S observation of 40 ks performed in FAINT mode, kindly provided to us by P. Tozzi.

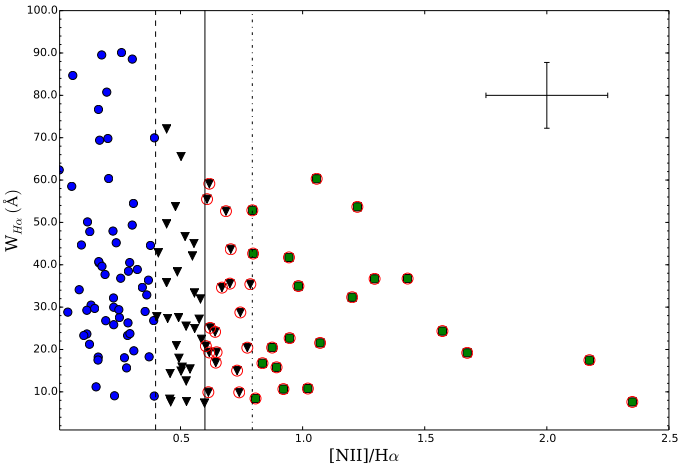

Fig. 11. EWαn2 diagram showing pure SF galaxies according to S06 criterion (blue dots), pure K01 AGN (green squares) and composite SF+AGN objects (black triangles). Classical AGNs as defined by H97 are denoted by open red circles. The dashed vertical line corresponds to S06 separation criterion, the solid one to the H97 boundary, and finally the dashed-dotted line marks the K01 boundary. The error bars in the top right corner correspond to the median errors within our sample of ELG.

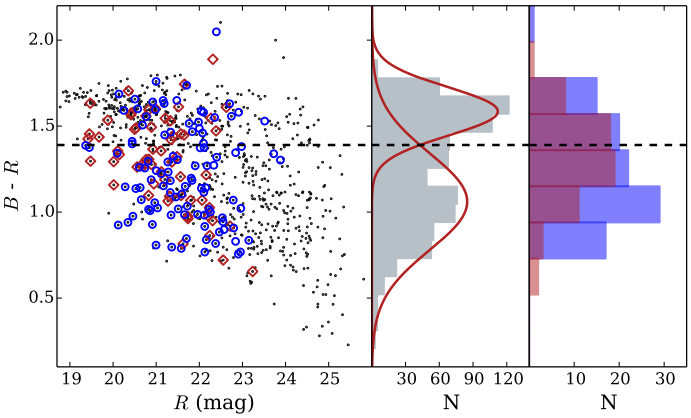

Fig. 12. *Left*: $B-R$ vs. R colour–magnitude diagram. The AGN are represented by red diamond symbols, while blue circles are SF galaxies. The black dots represent the cluster control sample from M05. The dashed line corresponds to the separation between the red sequence and blue cloud populations (see text). *Middle*: histogram of the control sample. The bi-modality of the distribution of optical colours is evident. The red curves are the best Gaussian fits to the distribution. *Right*: colour histograms for AGNs (red) and SF (blue) galaxies. It is likely that both populations are drawn from different distributions.

Five sources (out of 37) have been ascribed to the cluster after cross-matching the X-ray emitter list with the catalogue of spectroscopic redshifts from M05. From these, three sources have been detected as ELG in our survey and have been classified as pure AGN or composite according to the [N II]/Hα ratio. The remaining two sources are detected in our deep TF images, but their pseudo-spectra do not show emission line features at a significant level of detection.

For the H97 SF galaxies, we computed the SFR using the standard assumption of one magnitude of extinction at the Hα line (Kennicutt 1992, in a forthcoming paper a more realistic estimation will be done using the Balmer decrement computed with the Hβ flux) and applying the standard luminosity-SFR conversion from Kennicutt (1998). The histogram of the SFR distribution is depicted in Fig. 5 (right panel). The SFR peaks at 0.8 $M_\odot$ yr^{-1} with a median value of 1.4 $M_\odot$ yr^{-1}.

The spatial distribution of AGN and SF galaxies in the radial velocity/projected cluster-centric distance space is depicted in Fig. 8. The very central region ($r \lesssim 250$ Kpc) is almost devoid of ELG, indicating an almost complete quenching of the star formation or AGN activity. AGNs are observed in both cluster components (A and B as defined in Sect. 6), but are more abundant in the main structure. Beyond this point, the analysis of the distribution of galaxies relative to the cluster-centric distance has a limited validity, since on the one hand, it does not account for the limited area coverage of our observations at large radii, and on the other, it does not provide information about the importance of star formation or AGN activity relative to the density of galaxies in the surrounding environment. A thorough analysis of the dependency of the SFR and specific SFR with the local galaxy density (characterised by the Σ_5 parameter) will be presented in Pérez-Martínez et al. (in prep.).

Finally, we plotted the colour–magnitude diagram (CMD) for the ELG sample, along with a control sample of cluster galaxies from M05. This control sample, comprising 792 galaxies, was drawn from the main catalogue by choosing all the objects having valid *BR* photometry, within the same sky area as our sample and fulfilling $0.35 < z < 0.45$ (either spectroscopic or photometric). The K-correction was applied to the M05 magnitudes by means of `kcorrect v4_2` (Blanton & Roweis 2007). The rest-frame $B-R$ vs. R CMD is depicted in Fig. 12. The bi-modality in the distribution of optical colours is clearly noticed, with a well developed red sequence. We defined a boundary between the red sequence and the blue cloud as the intersection of the Gaussian functions resulting from the fit to each colour peak ($B-R = 1.39$). We investigated the colour distributions of AGNs and SF galaxies (right panel in Fig. 12). The differences are not outstanding but noticeable. The Kolmogorov-Smirnov test rejects the null hypothesis that both samples are drawn from the same distribution with a p-value of 0.09. The colour distribution of SF galaxies reaches a clear maximum in the blue cloud, with a tail towards the red sequence region (either due to dust absorption or to the presence of old, red stellar populations), while the AGN colour distribution tends to peak at the boundary between the two regions, the so-called "green valley", as expected for the population of galaxies hosting active nuclei (see for instance Pović et al. 2012, and references therein).

9. Cluster dynamics from emission line galaxies

As a final test of the reliability and usefulness of our data beyond the main drivers of the GLACE survey, we applied the caustic technique (Diaferio & Geller 1997; Diaferio 1999) using the `CausticApp` code (Serra & Diaferio, in prep.) to explore the possibility of using ELG radial velocity data to trace the cluster mass. Unlike the traditional Jeans approach, this method does not rely on the assumption of dynamical equilibrium and can be used to estimate the cluster mass even in non-equilibrium regions. Thus, in principle, it is well suited to being applied to ELGs, which are very likely not in dynamical equilibrium.

To briefly summarise the physical idea behind the caustic technique, we follow Serra et al. (2011): in hierarchical clustering models of structure formation, clusters form by the aggregation of smaller systems. This accretion does not take place purely radially, but particles within the falling clumps have velocities with a substantial non-radial component. The rms velocity $\langle v^2 \rangle$ is due to the gravitational potential of the cluster and the groups

where the galaxies reside, as well as to the tidal fields of the surrounding region.

In a redshift diagram (i.e. line-of-sight velocity v_{los} vs. projected distance to the centre R_p), cluster galaxies populate a region with a characteristic trumpet shape with decreasing amplitude $\mathcal{A}(R_p)$ with increasing R_p. This amplitude is related to $\langle v^2 \rangle$. Diaferio & Geller (1997) identified this amplitude with the average component along the line of sight of the escape velocity at the three-dimensional radius $r = R_p$. The projection along the line of sight involves a function that depends on the anisotropy parameter $\beta(r) = 1 - (\langle v_\theta^2 \rangle + \langle v_\phi^2 \rangle)/2\langle v_r^2 \rangle$. Here, $\langle v_\theta^2 \rangle$, $\langle v_\phi^2 \rangle$, and $\langle v_r^2 \rangle$ are the longitudinal, azimuthal, and radial components of the velocity $\boldsymbol{v}$ of a galaxy, respectively, and the brackets represent the average over a local volume at a given position $\boldsymbol{r}$. Considering the cluster rotation negligible, $\langle v_\theta^2 \rangle = \langle v_\phi^2 \rangle = \langle v_{los}^2 \rangle$, where $\langle v_{los}^2 \rangle$ is the line-of-sight component of the velocity.

Following the results of Diaferio & Geller (1997), the square of the caustic amplitude $\mathcal{A}^2(\mathrm{r}) = \langle v_{esc,los}^2 \rangle$ and relating the escape velocity to the cluster gravitational potential as $\langle v_{esc}^2 \rangle = -2\phi(\mathrm{r})$, it can be shown that

$$GM(<r) = \int_0^r \mathcal{A}^2(\mathrm{r}) g(\beta) \mathcal{F}(r)\, \mathrm{d}r \tag{13}$$

where $\mathcal{F}(r) = -2\pi G\rho(r)r^2/\phi(r)$, with $\rho(\mathrm{r})$ the mass density profile and $g(\beta) = (3 - 2\beta(\mathrm{r}))/(1 - \beta(r))$. To solve Eq. (13), it is assumed that the product $\mathcal{F}_\beta(r) = \mathcal{F}(r)g(\beta)$ varies slowly with r, so it is possible to replace it by a constant parameter $\mathcal{F}_\beta$. It is easy to show that $\mathcal{F}(r)$ is a slowly varying function of r in hierarchical clustering scenarios. The assumption that $\mathcal{F}_\beta(r)$ is also a slow function of r is somewhat stronger and is demonstrated in Serra et al. (2011).

Therefore, the mass profile could be estimated as

$$GM(<r) = \mathcal{F}_\beta \int_0^{\mathrm{r}} \mathcal{A}^2(r)\, \mathrm{d}r. \tag{14}$$

The `CausticApp` is a graphical interface that allows easy use of the caustic technique. The technique uses a binary tree according to a hierarchical method of arranging the galaxies in a catalogue according to their projected binding energy. By cutting the tree at the appropriate thresholds (details in Serra et al. 2011), it provides a set of candidate members, the cluster centre, velocity dispersion, and size. With that information, a redshift diagram is created and the caustics located. Finally, the caustic mass profile is estimated.

We ran the code with our complete data set of 174 ELGs, setting a conservative filling factor $\mathcal{F}_\beta = 0.5$. The centre of the cluster computed by the code is $\alpha_{ELG} = 0^h26^m40.8^s$, $\delta_{ELG} = 17°9'21.6''$, and the final members are 121. The redshift diagram with the location of the caustics and the cluster mass profile are depicted in the left- and right-hand panels of Fig. 13, respectively.

Figure 13 also shows two other mass profiles estimated from ZwCl 0024.0+1652 data: a weak-lensing mass profile from Kneib et al. (2003) and another caustic mass profile, obtained with the larger galaxy catalogue with 333 galaxies within the redshift range $z = [0.35,0.45]$ used by Diaferio et al. (2005). For this analysis we kept the cluster centre used in Diaferio et al. (2005): $\alpha_{D05} = 0^h26^m45.9^s$, $\delta_{D05} = 17°9'41.1''$. The number of members identified in this case is 251. Despite the number difference, our sample is able to yield a very good estimate of the centre. Indeed, the offset between $(\alpha_{ELG}, \delta_{ELG})$ and $(\alpha_{D05}, \delta_{D05})$ is negligible.

The agreement among all of the three mass profiles is remarkable at $r = [1,2.3]$ Mpc h^{-1}. In the inner regions, the ELG-caustic mass profile is considerably lower than the other two, owing to the lack of galaxies in the very central regions of the cluster. In most clusters, ELGs avoid the cluster centre, which translates into a caustic amplitude that tends to underestimate the mass profile in the inner regions. As the mass profile is cumulative, this underestimate propagates into the final mass estimates. However, the cumulative caustic mass profile from ELGs in Fig. 13 shows that the central mass does not contribute substantially to the total cluster mass at large radii. This suggests that in this cluster the velocity field is well sampled by the ELGs in the outskirts; consequently, the ELG-caustic mass profile is consistent with the estimates from previous studies.

With the caustic method, we derive $r_{200} = (1.21 \pm 0.1)$ Mpc h^{-1} and $M_{200} = (4.1 \pm 0.2) \times 10^{14}\, M_\odot\, h^{-1}$, where the uncertainties are due to the uncertainties in the mass profile. For comparison, Kneib et al. (2003), from weak-lensing analysis, derived $r_{200} = (1.19 \pm 0.9)$ Mpc h^{-1} and $M_{200} = (3.97^{+0.8}_{-0.7}) \times 10^{14}\, M_\odot\, h^{-1}$. Therefore, there is very good agreement between our results and those obtained by means of a radically different approach.

10. Summary and conclusions

Aimed at exploring the technical feasibility of the GLACE project, we carried out a TF survey of the intermediate redshift cluster ZwCl 0024.0+1652 (Cl0024 hereafter) at $z = 0.395$, targetting the Hα/[N II] line complex. We performed two pointings, covering approximately two virial radii and a velocity field of approximately ±4000 km s^{-1}. Cl0024 is a very well studied cluster, and hence a good test bench to explore the capabilities, performance, and limitations of the TF tomography method. In this paper we present the main technical aspects related to the creation of the catalogue of Hα emitters, along with some simulations aimed at confirming the validity (and limitations) of our methods. We present a set of scientific results that can be used as a benchmark of the performance of our techniques upon comparison with previous works. These results include the spatial and redshift distribution of cluster galaxies, the Hα luminosity function, the population of star-forming (SF) galaxies and AGNs, and finally, an attempt to estimate the mass and velocity dispersion of the cluster based on our emission line data. The main results are

- A catalogue of 174 unique cluster emitters has been compiled. The completeness limit of our Hα line sample is $f_{H\alpha} \sim 0.9 \times 10^{-16}$ erg s^{-1} cm^{-2}, a flux consistent with or below the GLACE requirement.
- We have compared our redshift estimates for our galaxies, as given by the Hα line position in the pseudo-spectra, with spectroscopic redshifts from Moran et al. (2005). There is excellent agreement: the redshift error defined as $|z_{TF} - z_{spec}|/(1 + z_{spec})$ is on average 0.002 (median value 0.0005) with a maximum value of 0.02. We can therefore consider the TF-derived redshifts as having spectroscopic quality.
- The redshift distribution of the cluster galaxies allows us to identify two interacting structures already identified in spectroscopic surveys (Czoske et al. 2002). Moreover, we suggest the existence of a third interacting group (previously not identified as such, but as part of the surrounding field galaxy population), although the clustering of the sources can be due to an instrumental effect (uneven spatial coverage at the shortest and longest wavelengths).

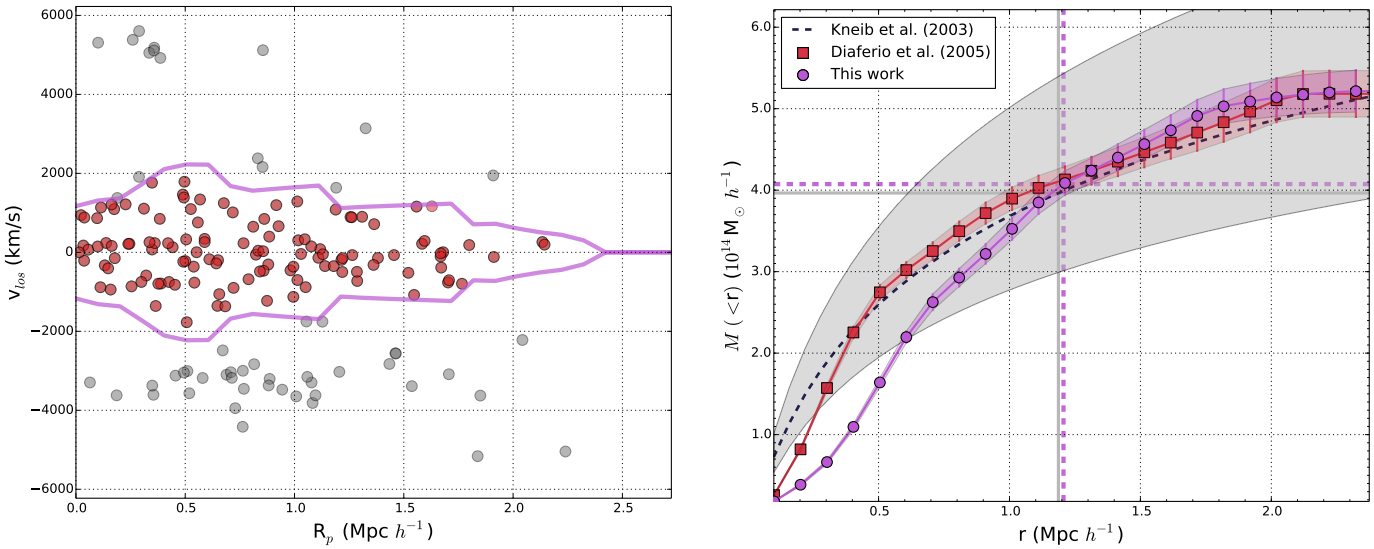

Fig. 13. *Left*: redshift diagram showing the selected cluster members (red dots, coincident with those in the main structure identified in Sect. 6) and the caustics (purple solid lines). *Right*: caustic-ELG mass profile (purple circles) computed by integrating the squared caustic amplitude profile; NFW-best-fit mass profile to the weak-lensing mass from Kneib et al. (2003; black dashed line); caustic analysis of the catalog from Diaferio et al. (2005; red squares). The vertical and horizontal lines are M_{200} and r_{200} of the caustic-ELG (purple) and weak-lensing (grey) mass profiles.

- The Hα luminosity function is well aligned with previous estimates from Kodama et al. (2004) up to the completeness limit of the sample, $\log L(\mathrm{H}\alpha{+}[\mathrm{N\,II}])\,(\mathrm{erg\ s^{-1}}) \simeq 41$.
- Broad-line AGNs (BLAGN) can be separated from narrow-line ones (NLAGN) or SF galaxies. To select candidates to BLAGN, we performed simple Gaussian fits to the pseudo-spectra, arriving at a final list of 25 robust candidates, i.e. 14% of the sample of ELGs. Furthermore, our observing technique allowed us to deblend the Hα and [N II] lines. In fact, in an outstanding portion of the objects, both lines appear to be clearly separated even in a visual inspection of the pseudo-spectra. We have used this deblending capability to discriminate the population of NLAGNs from the SF galaxies. The number of NLAGNs depends on the criterion used. If a "classical" separation criterion is applied (Ho et al. 1997, H97), the fraction of NLAGNs is ∼22%. The total percentage of AGN (BLAGN+NLAGN) is ∼37% or around 17% of the cluster population brighter than $R = 22.3$, so similar to estimates derived from [O II] observations $z \approx 0.9$. This suggests a lack of redshift evolution of the population of faint AGNs in the range $0.4 \lesssim z \lesssim 0.9$, or at least much milder than previous predictions.
- The SFR, which was computed using the standard assumption of one magnitude of extinction at the Hα line and the standard luminosity-SFR conversion from Kennicutt (1998), peaks at 0.8 $M_\odot\,\mathrm{yr^{-1}}$ with a median value of 1.4 $M_\odot\,\mathrm{yr^{-1}}$.
- We have found that the innermost region of the cluster ($r \lesssim 250$ kpc) is virtually devoid of ELGs, indicating an almost complete quenching of the star formation and AGN activity, as expected for a cluster at this redshift.
- We used the dynamical information (radial velocities) provided by our ELGs to estimate the mass, radius, and velocity dispersion of Cl0024 using the technique of caustics in the redshift space (Diaferio & Geller 1997; Diaferio 1999) as implemented in the `CausticApp` application from Serra et al. (2011). With the caustic method, we derive $r_{200} = (1.21 \pm 0.1)\,\mathrm{Mpc}\ h^{-1}$ and $M_{200} = (4.1 \pm 0.2) \times 10^{14}\,M_\odot\,h^{-1}$, in very good agreement with the weak-lensing estimate from Kneib et al. (2003).

The results outlined above indicate that the TF tomography technique is a powerful tool for the proposed research and that the devised observing methods and reduction and analysis procedures yield results that meet or exceed the GLACE requirements. The tunable filters of the OSIRIS instrument at the 10.4 m GTC telescope constitute a powerful tool for exploring galaxy clusters, allowing important properties of the members to be derived, and even allow investigating the cluster dynamics.

Acknowledgements. We acknowledge the support provided by M. Balogh during the preparation of the GLACE proposal to ESO, as well as his useful suggestions for improving the quality of this paper. We also acknowledge the anonymous referee. We acknowledge financial support from Spanish MINECO under grant AYA2014-29517-C03-01, AYA2011-29517-C03-02 and AYA2014-58861-C03. E.J.A. acknowledges support from MINECO under grant AYA2013-40611-P. J.M.R.E. acknowledges support from MINECO under grant AYA2012-39168-C03-01. We acknowledge support from the Faculty of the European Space Astronomy Centre (ESAC). I.R.S. acknowledges support from STFC GT/I001573/1, a European Research Council Advanced Programme Dustygal (321334) and a Royal Society/Wolfson Research Merit Award. J.S.S. acknowledges funding from the European Union Seventh Framework Programme (FP7/2007−2013) under grant agreement No. 267251 "Astronomy Fellowships in Italy" (AstroFIt). Based on observations made with the Gran Telescopio Canarias (GTC), installed at the Spanish Observatorio del Roque de los Muchachos of the Instituto de Astrofsica de Canarias, on the island of La Palma. This publication makes use of data products from the Two Micron All Sky Survey, which is a joint project of the University of Massachusetts and the Infrared Processing and Analysis Center/California Institute of Technology, funded by the National Aeronautics and Space Administration and the National Science Foundation.

References

Alloin, D., Collin-Souffrin, S., Joly, M., & Vigroux, L. 1979, A&A, 78, 200
Altieri, B., Berta, S., Lutz, D., et al. 2010, A&A, 518, L17
Arribas, S., Mediavilla, E., García-Lorenzo, B., & del Burgo, C. 1997, ApJ, 490, 227
Baldwin, J. A., Phillips, M. M., & Terlevich, R. 1981, PASP, 93, 5
Balogh, M. L., Morris, S. L., Yee, H. K. C., Carlberg, R. G., & Ellingson, E. 1999, ApJ, 527, 54
Balogh, M. L., Navarro, J. F., & Morris, S. L. 2000, ApJ, 540, 113
Bertin, E., & Arnouts, S. 1996, A&AS, 117, 393
Blanton, M. R., & Roweis, S. 2007, AJ, 133, 734
Bruzual, G., & Charlot, S. 2003, MNRAS, 344, 1000
Butcher, H., & Oemler, Jr., A. 1984, ApJ, 285, 426
Calzetti, D., Armus, L., Bohlin, R. C., et al. 2000, ApJ, 533, 682

Cepa, J., Aguiar, M., Bland-Hawthorn, J., et al. 2003, in Rev. Mex. Astron. Astrofis. Conf. Ser. 16, eds. J. M. Rodriguez Espinoza, F. Garzon Lopez, & V. Melo Martin, 13
Cepa, J., Aguiar, M., Castañeda, H. O., et al. 2005, in Rev. Mex. Astron. Astrofis. Conf. Ser. 24, eds. A. M. Hidalgo-Gámez, J. J. González, J. M. Rodríguez Espinosa, & S. Torres-Peimbert, 1
Cepa, J., Bongiovanni, A., Pérez García, A. M., et al. 2013, in Rev. Mex. Astron. Astrofis. Conf. Ser., 42, 70
Chabrier, G. 2003, PASP, 115, 763
Cid Fernandes, R., Stasińska, G., Schlickmann, M. S., et al. 2010, MNRAS, 403, 1036
Coia, D., Metcalfe, L., McBreen, B., et al. 2005, A&A, 430, 59
Czoske, O., Moore, B., Kneib, J., & Soucail, G. 2002, A&A, 386, 31
Denicoló, G., Terlevich, R., & Terlevich, E. 2002, MNRAS, 330, 69
Diaferio, A. 1999, MNRAS, 309, 610
Diaferio, A., & Geller, M. J. 1997, ApJ, 481, 633
Diaferio, A., Geller, M. J., & Rines, K. J. 2005, ApJ, 628, L97
Dressler, A. 1980, ApJ, 236, 351
Dressler, A., Oemler, Jr., A., Couch, W. J., et al. 1997, ApJ, 490, 577
Fernández Lorenzo, M., Cepa, J., Bongiovanni, A., et al. 2009, A&A, 496, 389
Filippenko, A., & Greenstein, J. L. 1984, PASP, 96, 530
García-Lorenzo, B., Sánchez, S. F., Mediavilla, E., González-Serrano, J. I., & Christensen, L. 2005, ApJ, 621, 146
Geach, J. E., Smail, I., Ellis, R. S., et al. 2006, ApJ, 649, 661
González, J. J., Cepa, J., González-Serrano, J. I., & Sánchez-Portal, M. 2014, MNRAS, 443, 3289
Haines, C. P., Smith, G. P., Egami, E., et al. 2009, ApJ, 704, 126
Haines, C. P., Pereira, M. J., Smith, G. P., et al. 2013, ApJ, 775, 126
Ho, L. C., Filippenko, A. V., & Sargent, W. L. W. 1997, ApJS, 112, 315
Ho, L. C., Feigelson, E. D., Townsley, L. K., et al. 2001, ApJ, 549, L51
Ilbert, O., Arnouts, S., McCracken, H. J., et al. 2006, A&A, 457, 841
Ilbert, O., Capak, P., Salvato, M., et al. 2009, ApJ, 690, 1236
Jones, D. H., & Bland-Hawthorn, J. 2001, ApJ, 550, 593
Jones, D. H., Shopbell, P. L., & Bland-Hawthorn, J. 2002, MNRAS, 329, 759
Kaspi, S., Maoz, D., Netzer, H., et al. 1996, ApJ, 470, 336
Kauffmann, G., Heckman, T. M., Tremonti, C., et al. 2003, MNRAS, 346, 1055
Kauffmann, G., White, S. D. M., Heckman, T. M., et al. 2004, MNRAS, 353, 713
Kennicutt, Jr., R. C. 1992, ApJ, 388, 310
Kennicutt, Jr., R. C. 1998, ARA&A, 36, 189
Kewley, L. J., Dopita, M. A., Sutherland, R. S., Heisler, C. A., & Trevena, J. 2001, ApJ, 556, 121
Kneib, J., Hudelot, P., Ellis, R. S., et al. 2003, ApJ, 598, 804
Kodama, T., & Bower, R. G. 2001, MNRAS, 321, 18
Kodama, T., Bell, E. F., & Bower, R. G. 1999, MNRAS, 302, 152
Kodama, T., Balogh, M. L., Smail, I., Bower, R. G., & Nakata, F. 2004, MNRAS, 354, 1103
Koyama, Y., Kodama, T., Shimasaku, K., et al. 2010, MNRAS, 403, 1611
Koyama, Y., Kodama, T., Nakata, F., Shimasaku, K., & Okamura, S. 2011, ApJ, 734, 66
Lara-López, M. A., Cepa, J., Castañeda, H., et al. 2010, PASP, 122, 1495
Lemaux, B. C., Lubin, L. M., Shapley, A., et al. 2010, ApJ, 716, 970
Madau, P., Pozzetti, L., & Dickinson, M. 1998, ApJ, 498, 106
Martini, P., Kelson, D. D., Mulchaey, J. S., & Trager, S. C. 2002, ApJ, 576, L109
Martini, P., Sivakoff, G. R., & Mulchaey, J. S. 2009, ApJ, 701, 66
Martini, P., Miller, E. D., Brodwin, M., et al. 2013, ApJ, 768, 1
Miller, C. J., Nichol, R. C., Gómez, P. L., Hopkins, A. M., & Bernardi, M. 2003, ApJ, 597, 142
Monet, D. G., Levine, S. E., Canzian, B., et al. 2003, AJ, 125, 984
Moran, S. M., Ellis, R. S., Treu, T., et al. 2005, ApJ, 634, 977
Moran, S. M., Ellis, R. S., Treu, T., et al. 2007, ApJ, 671, 1503
Oke, J. B. 1974, ApJS, 27, 21
Oke, J. B. 1990, AJ, 99, 1621
Pagel, B. E. J., Edmunds, M. G., Blackwell, D. E., Chun, M. S., & Smith, G. 1979, MNRAS, 189, 95
Pascual, S., Gallego, J., & Zamorano, J. 2007, PASP, 119, 30
Pérez-Martínez, R., Sánchez-Portal, M., Pintos-Castro, I., et al. 2013, Astron. Nachr., 334, 458
Pimbblet, K. A., Smail, I., Edge, A. C., et al. 2001, MNRAS, 327, 588
Pintos-Castro, I., Sánchez-Portal, M., Cepa, J., et al. 2013, A&A, 558, A100
Poggianti, B. M., Smail, I., Dressler, A., et al. 1999, ApJ, 518, 576
Popesso, P., & Biviano, A. 2006, A&A, 460, L23
Popesso, P., Biviano, A., Romaniello, M., & Böhringer, H. 2007, A&A, 461, 411
Pović, M., Sánchez-Portal, M., Pérez García, A. M., et al. 2012, A&A, 541, A118
Rousselot, P., Lidman, C., Cuby, J.-G., Moreels, G., & Monnet, G. 2000, A&A, 354, 1134
Roy, J.-R., Arsenault, R., & Joncas, G. 1986, ApJ, 300, 624
Serra, A. L., Diaferio, A., Murante, G., & Borgani, S. 2011, MNRAS, 412, 800
Skrutskie, M. F., Cutri, R. M., Stiening, R., et al. 2006, AJ, 131, 1163
Sorrentino, G., Radovich, M., & Rifatto, A. 2006, A&A, 451, 809
Stasińska, G., Cid Fernandes, R., Mateus, A., Sodré, L., & Asari, N. V. 2006, MNRAS, 371, 972
Taylor, M. B. 2005, in Astronomical Data Analysis Software and Systems XIV, eds. P. Shopbell, M. Britton, & R. Ebert, ASP Conf. Ser., 347, 29
Treu, T., Ellis, R. S., Kneib, J., et al. 2003, ApJ, 591, 53
Veilleux, S., & Osterbrock, D. E. 1987, ApJS, 63, 295
Webb, T. M. A., O'Donnell, D., Yee, H. K. C., et al. 2013, AJ, 146, 84
Zhang, Y.-Y., Böhringer, H., Mellier, Y., Soucail, G., & Forman, W. 2005, A&A, 429, 85

[1] European Space Astronomy Centre (ESAC)/ESA, PO Box 78, 28690 Villanueva de la Canada, Madrid, Spain
e-mail: miguel.sanchez@sciops.esa.int
[2] ISDEFE, Beatriz de Bobadilla 3, 28040 Madrid, Spain
[3] Instituto de Astrofísica de Canarias, 38205, La Laguna, 38701 La Laguna, Tenerife, Spain
[4] Universidad de La Laguna, 38207 Tenerife, Spain
[5] Instituto de Astrofísica de Andalucía, CSIC, 18080 Granada, Spain
[6] School of Physics and Astronomy, University of Nottingham, Nottingham NG7 2RD, UK
[7] GEPI, Observatoire de Paris & CNRS, 92195 Meudon, France
[8] Centro de Astrobiología, INTA-CSIC, 28850 Torrejón de Ardoz, Madrid, Spain
[9] INAF, Osservatorio Astronomico di Trieste, 34143 Trieste, Italy
[10] Department of Physics, University of Bristol, Bristol, BS8 1TH, UK
[11] Institut de Ciències de l'Espai (CSIC), 08193 Barcelona, Spain
[12] Instituto Polictécnico Nacional, 07738 México D.F., México
[13] Laboratoire AIM Saclay, CEA/IRFU, CNRS/INSU, Université Paris Diderot, 75014 Paris, France
[14] Department of Physics, McGill University, Montreal, H3A 2T8, Quebec, Canada
[15] Instituto de Física de Cantabria, CSIC-Univ. de Cantabria, 39005 Santander, Spain
[16] Departamento de Astronomía, Universidad de Chile, Casilla 36-D, Correo Central, Casilla 36-D, Correo Central, Santiago, Chile
[17] University College, Belfield, Dublin Bristol, BS8 1TH, Ireland
[18] INAF, Osservatorio Astronomico di Padova, 35122 Padova, Italy
[19] Institute for Computational Cosmology, Durham University, Durham DH1 3LE, UK
[20] Institute of Astro- and Particle Physics, University of Innsbruck, 6020 Innsbruck, Austria
[21] Centro de Estudios de Física del Cosmos de Aragón, 44001 Teruel, Spain
[22] Dipartimento di Fisica, Università degli Studi di Milano, 20133 Milano, Italy
[23] Dipartimento di Fisica, Università di Torino, 10125 Torino, Italy
[24] Istituto Nazionale di Fisica Nucleare (INFN), sezione di Torino, 10125 Torino, Italy
[25] Departamento de Astronomia, Instituto de Astronomia, Geofísica e Ciências Atmosféricas da USP, 1226 São Paulo, Brazil
[26] Institute for Astronomy, University of Edinburgh, Royal Observatory, Blackford Hill, Edinburgh, EH9 3HJ, UK
[27] European Southern Observatory, 85748 Garching, Germany
[28] INAF-Osservatorio Astrofisico di Arcetri, 50125 Florence, Italy
[29] Departamento de Astrofísica, Facultad de CC. Físicas, Universidad Complutense de Madrid, 28040 Madrid, Spain

Pages 20 to 22 are available in the electronic edition of the journal at http://www.aanda.org

Table 5. Catalogue of unique ELGs of Cl0024.

ID	RA J2000 (00:26:ss.ss)	Dec J2000 (+17:mm:ss.s)	z	$f_{H\alpha}$ 10^{-17} (erg cm^{-2} s^{-1})	$f_{[NII]}$ 10^{-17} (erg cm^{-2} s^{-1})	$EW_{H\alpha}$ (Å)	$EW_{H\alpha+[NII]}$ (Å)	Type
4_C	34.27	06:04.5	0.3820	33 ± 6	2 ± 2	84.7	88.9	SF
12_C	42.98	06:12.2	0.3999	18 ± 6	–	38.9	–	BLAGN
24_C	28.93	06:20.8	0.3982	7 ± 3	5 ± 3	9.9	15.6	NLAGN
35_C	23.84	06:26.9	0.3955	10 ± 6	4 ± 4	9.0	12.3	SF
60_C	38.72	06:46.9	0.3967	12 ± 3	–	42.3	–	SF
70_C	29.05	06:59.1	0.3785	10 ± 4	5 ± 7	17.9	26.4	SF
72_C	19.39	07:03.0	0.3993	35 ± 11	18 ± 10	17.4	26.6	BLAGN
73_C	42.31	07:04.7	0.3949	7 ± 2	8 ± 2	36.7	87.2	NLAGN
87_C	14.95	07:14.5	0.3803	13 ± 5	14 ± 8	21.6	43.6	NLAGN
96_C	34.49	07:15.4	0.3832	37 ± 11	–	35.5	–	SF
97_C	34.88	07:15.4	0.4014	10 ± 3	5 ± 3	14.9	22.3	SF
105_C	14.79	07:19.8	0.3832	60 ± 14	–	62.4	–	SF
106_C	30.99	07:22.0	0.3807	25 ± 7	6 ± 4	30.0	36.5	SF
138_C	34.22	07:42.8	0.3812	33 ± 8	12 ± 6	36.4	49.3	SF
143_C	39.26	07:46.5	0.3784	14 ± 4	1 ± 3	34.1	36.9	SF
147_C	41.17	07:47.0	0.3888	13 ± 3	2 ± 2	40.5	46.5	SF
153_C	21.48	07:55.0	0.3774	16 ± 5	11 ± 5	43.7	75.2	NLAGN
163_C	44.93	08:10.1	0.3955	25 ± 18	22 ± 19	6.7	12.7	BLAGN
193_C	40.10	08:21.8	0.4008	6 ± 2	4 ± 5	15.0	26.0	NLAGN
196_C	27.09	08:23.8	0.3812	15 ± 6	13 ± 9	15.8	30.0	NLAGN
200_C	42.90	08:23.8	0.3962	11 ± 3	8 ± 5	35.6	58.8	NLAGN
219_C	29.81	08:36.4	0.3993	59 ± 15	21 ± 10	62.1	81.3	BLAGN
224_C	16.48	08:40.3	0.3943	7 ± 1	2 ± 2	44.6	59.5	SF
227_C	35.73	08:40.6	0.4003	13 ± 3	16 ± 7	32.3	70.4	NLAGN
246_C	23.79	08:49.9	0.4002	17 ± 6	5 ± 9	15.7	20.0	SF
253_C	23.79	08:50.2	0.3810	19 ± 4	6 ± 3	54.5	69.7	SF
255_C	38.29	08:51.4	0.4007	7 ± 2	3 ± 1	49.7	70.0	SF
263_C	27.70	08:51.5	0.3991	48 ± 9	30 ± 11	59.1	90.7	NLAGN
265_C	33.82	08:56.0	0.4002	16 ± 3	8 ± 3	47.7	67.8	BLAGN
280_C	33.83	08:56.6	0.3910	11 ± 3	11 ± 6	22.7	44.0	NLAGN
285_C	18.64	08:57.1	0.3935	101 ± 14	5 ± 3	425.6	437.2	SF
287_C	18.63	08:57.1	0.3942	42 ± 15	12 ± 8	23.3	29.9	SF
290_C	42.37	09:02.2	0.3798	6 ± 3	4 ± 2	16.9	28.0	SF
293_C	30.79	09:02.5	0.4008	4 ± 1	7 ± 3	24.3	62.9	NLAGN
297_C	11.22	09:02.7	0.3962	31 ± 12	32 ± 21	12.1	24.5	NLAGN
303_C	30.80	09:02.9	0.3870	5 ± 2	–	28.3	–	BLAGN
308_C	37.99	09:04.4	0.3995	40 ± 7	8 ± 4	69.8	82.3	SF
314_C	41.09	09:05.3	0.3959	6 ± 2	1 ± 2	30.5	34.5	SF
317_C	19.72	09:10.2	0.4009	10 ± 3	6 ± 2	22.4	35.6	SF
320_C	40.69	09:11.9	0.4002	14 ± 3	–	89.2	–	SF
322_C	43.27	09:12.6	0.4034	9 ± 3	–	35.5	–	SF
323_C	43.79	09:14.3	0.3959	8 ± 2	–	64.4	–	SF
332_C	34.29	09:14.5	0.3811	23 ± 5	9 ± 5	70.0	92.1	SF
337_C	30.97	09:14.7	0.3985	7 ± 2	5 ± 2	81.3	128.9	BLAGN
338_C	40.31	09:15.7	0.3915	28 ± 9	14 ± 10	15.8	23.9	SF
339_C	31.64	09:16.0	0.3902	13 ± 4	4 ± 2	38.5	48.8	SF
341_C	28.14	09:16.1	0.3937	27 ± 8	21 ± 16	20.4	36.7	NLAGN
343_C	15.28	09:17.8	0.3992	30 ± 6	18 ± 5	55.5	90.5	NLAGN
345_C	18.26	09:17.9	0.3955	18 ± 5	10 ± 4	25.5	38.4	SF
353_C	18.25	09:17.9	0.3951	10 ± 2	5 ± 2	38.4	55.6	SF
358_C	15.25	09:18.2	0.4193	8 ± 3	–	26.5	–	SF
359_C	41.15	09:18.6	0.4202	16 ± 5	–	48.9	–	SF
364_C	28.52	09:20.5	0.4212	7 ± 3	–	35.7	–	SF
366_C	28.52	09:20.9	0.3992	67 ± 12	17 ± 8	90.1	109.3	SF
374_C	31.31	09:22.4	0.4187	6 ± 3	–	12.8	–	SF
382_C	33.50	09:23.7	0.4040	8 ± 2	4 ± 3	25.0	38.3	SF
388_C	40.08	09:24.1	0.3783	11 ± 3	1 ± 2	58.5	61.5	SF
405_C	32.32	09:24.2	0.3936	114 ± 30	66 ± 24	27.1	42.1	SF
408_C	33.51	09:24.3	0.3943	70 ± 25	34 ± 14	21.0	31.2	NLAGN
409_C	35.93	09:24.5	0.3958	26 ± 16	21 ± 12	8.4	15.2	SF
410_C	40.99	09:24.6	0.3930	11 ± 4	2 ± 5	18.2	21.0	SF

Notes. The identifiers with "C" correspond to sources gathered from the central pointing, while those with "O" correspond to sources gathered from the offset one.

Table 5. continued.

ID	RA J2000 (00:26:ss.ss)	Dec J2000 (+17:mm:ss.s)	z	$f_{H\alpha}$ 10^{-17} (erg cm^{-2} s^{-1})	$f_{[NII]}$ 10^{-17} (erg cm^{-2} s^{-1})	$EW_{H\alpha}$ (Å)	$EW_{H\alpha+[NII]}$ (Å)	Type
422_C	34.09	09:26.0	0.3933	67 ± 14	37 ± 12	45.1	68.1	SF
423_C	35.39	09:26.3	0.4199	14 ± 5	–	38.3	–	SF
424_C	24.34	09:26.6	0.3908	51 ± 10	21 ± 9	42.8	59.1	SF
433_C	24.34	09:26.9	0.4004	13 ± 3	2 ± 2	47.8	53.2	SF
437_C	39.84	09:28.7	0.4189	23 ± 10	-	44.6	–	SF
443_C	42.44	09:32.2	0.3961	12 ± 3	4 ± 5	29.0	39.7	SF
450_C	34.55	09:32.8	0.3942	12 ± 3	3 ± 2	45.2	55.0	SF
451_C	35.48	09:36.0	0.3911	25 ± 7	5 ± 4	26.8	31.8	SF
452_C	44.08	09:37.9	0.3945	21 ± 8	8 ± 10	18.3	24.8	SF
453_C	39.85	09:45.5	0.4016	6 ± 3	3 ± 3	7.7	11.2	SF
456_C	24.84	09:47.2	0.3966	52 ± 13	48 ± 20	31.9	58.5	BLAGN
559_C	40.91	09:48.5	0.3870	7 ± 3	9 ± 6	10.1	23.0	BLAGN
560_C	18.15	09:48.7	0.3945	29 ± 6	13 ± 5	72.1	99.9	SF
571_C	18.15	09:48.7	0.3783	10 ± 2	3 ± 2	36.8	46.0	SF
574_C	38.61	09:50.9	0.3928	10 ± 2	2 ± 1	76.7	87.9	SF
575_C	42.63	09:51.2	0.3953	11 ± 2	2 ± 1	80.8	94.5	SF
582_C	41.37	09:51.4	0.3957	15 ± 4	3 ± 2	37.7	44.6	SF
612_C	34.45	09:52.2	0.3945	25 ± 6	12 ± 6	53.1	75.4	BLAGN
620_C	44.70	09:52.9	0.4062	9 ± 5	2 ± 4	9.1	11.1	SF
625_C	41.90	09:53.3	0.3964	5 ± 2	1 ± 1	29.3	32.6	SF
640_C	28.87	09:56.8	0.3930	11 ± 3	3 ± 5	27.5	34.4	SF
645_C	28.88	09:57.3	0.3794	20 ± 5	3 ± 2	89.5	103.2	SF
658_C	38.39	09:59.1	0.3950	7 ± 2	6 ± 3	35.4	64.9	NLAGN
659_C	36.85	10:00.2	0.3962	13 ± 3	14 ± 4	60.3	118.0	NLAGN
662_C	39.02	10:02.3	0.4181	9 ± 3	-	30.9	–	SF
675_C	32.00	10:02.6	0.3941	72 ± 15	22 ± 8	49.4	63.3	SF
677_C	16.92	10:02.8	0.3914	51 ± 19	41 ± 38	13.3	24.0	BLAGN
687_C	22.02	10:05.6	0.3917	13 ± 4	21 ± 9	19.2	51.6	NLAGN
714_C	24.51	10:06.4	0.3962	27 ± 6	14 ± 4	46.7	69.9	SF
728_C	31.25	10:11.2	0.3935	15 ± 4	14 ± 5	46.1	84.5	BLAGN
730_C	28.51	10:12.5	0.3993	7 ± 3	3 ± 3	26.8	36.4	SF
748_C	31.07	10:16.4	0.3798	24 ± 5	12 ± 7	65.6	91.9	SF
758_C	24.84	10:21.9	0.3959	22 ± 6	21 ± 8	35.0	67.7	NLAGN
762_C	32.72	10:24.9	0.3945	10 ± 3	4 ± 2	27.7	38.7	SF
763_C	25.86	10:26.8	0.3746	15 ± 8	36 ± 21	7.6	26.5	NLAGN
772_C	25.87	10:27.1	0.3982	16 ± 5	2 ± 2	50.1	55.6	SF
773_C	33.90	10:27.2	0.3949	30 ± 7	3 ± 6	104.5	114.0	SF
775_C	33.91	10:27.7	0.3918	8 ± 2	1 ± 1	40.7	46.9	SF
777_C	30.83	10:29.1	0.3805	46 ± 8	14 ± 4	88.6	111.1	SF
783_C	30.84	10:29.6	0.4011	6 ± 3	4 ± 4	7.4	11.8	SF
794_C	25.97	10:30.1	0.3768	16 ± 5	-	55.9	–	SF
811_C	37.98	10:31.3	0.4028	4 ± 1	6 ± 2	36.7	89.2	NLAGN
814_C	28.49	10:36.0	0.3782	7 ± 3	-	28.8	–	SF
826_C	37.30	10:37.0	0.3962	33 ± 7	26 ± 9	52.9	91.5	NLAGN
850_C	12.84	10:37.1	0.3919	64 ± 13	60 ± 18	41.7	83.2	NLAGN
869_C	42.74	10:43.3	0.3948	11 ± 3	6 ± 3	30.5	48.3	BLAGN
872_C	33.63	10:45.7	0.3935	7 ± 3	3 ± 2	12.6	19.0	SF
875_C	43.49	10:47.0	0.3899	31 ± 6	6 ± 4	60.4	71.1	SF
882_C	22.10	10:49.1	0.4052	7 ± 4	3 ± 4	8.3	12.0	SF
884_C	28.79	10:49.9	0.3967	14 ± 3	3 ± 4	48.0	57.0	SF
886_C	28.80	10:50.2	0.3938	7 ± 2	9 ± 2	53.7	117.4	NLAGN
888_C	43.31	10:51.5	0.3888	17 ± 3	11 ± 5	52.6	90.6	NLAGN
889_C	41.50	11:02.3	0.3952	9 ± 3	6 ± 3	24.2	40.3	NLAGN
907_C	39.14	11:02.6	0.4190	15 ± 5	–	55.5	–	SF
916_C	26.71	11:02.6	0.3836	4 ± 1	1 ± 1	26.3	33.2	SF
923_C	26.71	11:02.9	0.4035	4 ± 2	2 ± 3	7.7	11.8	SF
927_C	37.32	11:03.3	0.3967	34 ± 7	27 ± 8	42.7	78.8	NLAGN
929_C	26.38	11:04.7	0.3806	32 ± 11	15 ± 9	14.4	20.9	SF
935_C	26.37	11:05.1	0.3929	9 ± 3	3 ± 3	23.7	30.1	SF
938_C	36.58	11:08.1	0.3991	4 ± 1	2 ± 1	27.5	40.9	SF
948_C	35.16	11:08.4	0.3910	14 ± 3	1 ± 2	44.7	48.5	SF
953_C	35.16	11:09.0	0.3924	5 ± 2	10 ± 3	17.5	56.2	NLAGN
955_C	43.18	11:10.6	0.3910	9 ± 3	5 ± 4	19.3	32.0	NLAGN
966_C	22.81	11:13.1	0.3963	43 ± 9	24 ± 7	42.1	64.5	SF
977_C	30.98	11:14.2	0.3917	8 ± 2	7 ± 3	20.5	38.2	NLAGN

Table 5. continued.

ID	RA J2000 (00:26:ss.ss)	Dec J2000 (+17:mm:ss.s)	z	$f_{H\alpha}$ 10^{-17} (erg cm^{-2} s^{-1})	$f_{[NII]}$ 10^{-17} (erg cm^{-2} s^{-1})	$EW_{H\alpha}$ (Å)	$EW_{H\alpha+[NII]}$ (Å)	Type
72_O	25.46	11:27.2	0.3962	27 ± 4	6 ± 3	33.0	39.7	BLAGN
102_O	24.51	11:30.1	0.4020	28 ± 3	27 ± 6	17.1	32.9	BLAGN
139_O	27.95	11:38.0	0.3869	14 ± 2	3 ± 2	25.9	31.5	SF
146_O	33.89	11:42.4	0.3913	20 ± 2	12 ± 3	51.9	80.1	BLAGN
247_O	25.21	11:47.6	0.4016	24 ± 11	25 ± 8	137.1	147.1	SF
277_O	19.69	11:54.1	0.3928	9 ± 2	6 ± 3	34.6	57.0	NLAGN
278_O	19.68	11:54.4	0.3987	95 ± 7	113 ± 8	27.6	61.1	BLAGN
282_O	28.20	11:55.5	0.3802	9 ± 1	1 ± 1	23.7	26.4	SF
288_O	31.32	11:56.7	0.3916	9 ± 1	6 ± 1	16.8	27.2	BLAGN
291_O	25.68	12:05.4	0.3888	9 ± 2	6 ± 3	19.3	32.4	NLAGN
335_O	25.68	12:05.7	0.3941	9 ± 1	8 ± 3	10.6	19.9	NLAGN
336_O	33.64	12:19.7	0.3795	9 ± 2	2 ± 2	18.0	22.8	SF
381_O	07.54	12:29.9	0.3804	9 ± 2	1 ± 2	21.2	23.9	SF
384_O	31.25	12:32.1	0.3927	12 ± 2	2 ± 1	45.5	52.7	BLAGN
410_O	39.92	12:36.7	0.3810	7 ± 2	6 ± 3	16.8	30.9	NLAGN
457_O	20.48	12:45.4	0.3920	11 ± 2	8 ± 2	9.9	17.2	NLAGN
485_O	41.88	12:45.6	0.3935	10 ± 1	6 ± 1	31.9	50.7	SF
501_O	28.37	12:46.8	0.3790	7 ± 1	1 ± 1	11.2	12.9	SF
567_O	12.54	12:54.0	0.3970	10 ± 2	6 ± 2	25.1	39.8	NLAGN
568_O	37.59	12:54.3	0.3791	12 ± 2	–	28.9	–	SF
647_O	18.28	13:01.0	0.3794	9 ± 2	1 ± 2	17.5	20.6	SF
651_O	26.98	13:03.7	0.3946	15 ± 2	9 ± 3	19.2	31.7	BLAGN
657_O	28.23	13:07.8	0.3894	16 ± 2	7 ± 3	27.3	39.5	SF
664_O	28.24	13:07.9	0.3953	15 ± 2	9 ± 2	20.8	33.7	NLAGN
689_O	09.06	13:16.1	0.4098	8 ± 1	1 ± 2	39.6	46.3	SF
700_O	14.38	13:19.9	0.3808	10 ± 1	10 ± 3	10.8	21.6	NLAGN
708_O	36.16	13:36.4	0.3965	7 ± 1	2 ± 2	19.7	25.5	SF
847_O	15.40	13:41.7	0.3964	38 ± 7	–	51.9	–	SF
919_O	27.70	13:49.8	0.3952	14 ± 2	3 ± 2	29.4	36.5	SF
967_O	23.58	13:58.0	0.3783	8 ± 1	–	27.8	–	SF
998_O	23.62	13:58.5	0.3916	28 ± 2	26 ± 5	38.5	71.1	BLAGN
1015_O	29.19	14:02.9	0.3937	47 ± 3	14 ± 4	40.5	51.5	SF
1039_O	29.14	14:03.0	0.3961	28 ± 3	22 ± 5	23.2	41.1	BLAGN
1057_O	41.25	14:04.2	0.3934	13 ± 1	5 ± 1	32.9	44.7	SF
1074_O	37.75	14:12.2	0.3711	21 ± 2	12 ± 5	33.4	51.1	SF
1097_O	08.54	14:58.7	0.3947	9 ± 1	4 ± 2	53.8	76.4	SF
1103_O	20.14	15:10.5	0.3960	9 ± 2	1 ± 2	29.7	34.0	SF
1125_O	08.95	15:10.7	0.3914	8 ± 1	6 ± 3	28.7	48.9	NLAGN
1130_O	24.16	15:27.5	0.3919	8 ± 1	3 ± 1	34.7	46.5	SF
1133_O	32.95	15:29.3	0.3717	15 ± 3	2 ± 4	23.3	25.7	SF
1157_O	20.26	15:32.5	0.4042	54 ± 4	9 ± 3	69.4	80.1	SF
1162_O	28.36	15:36.1	0.3848	78 ± 8	34 ± 9	29.4	41.4	BLAGN
1165_O	18.65	15:42.7	0.3950	17 ± 2	9 ± 2	15.4	23.8	SF
1168_O	24.75	15:48.8	0.4005	13 ± 3	2 ± 2	19.8	22.4	BLAGN
1173_O	30.79	15:53.9	0.3901	18 ± 2	6 ± 4	38.9	50.6	SF
1204_O	26.10	16:47.0	0.3948	9 ± 2	2 ± 2	32.2	38.8	SF
1219_O	13.33	16:54.8	0.3820	17 ± 2	9 ± 2	22.3	33.7	BLAGN
1220_O	20.28	17:03.5	0.4006	14 ± 1	6 ± 1	35.8	50.6	SF